Internal Torques and Forces in Gyrostats with Magnetically Suspended Rotors

by
Marcus Carl Pressl

Thesis submitted to the Faculty of the
Virginia Polytechnic Institute and State University
in partial fulfillment of the requirements for the degree of

Master of Science
in
Aerospace Engineering

Dr. Christopher D. Hall, Committee Chair
Dr. Mary Kasarda, Committee Member
Dr. Craig Woolsey, Committee Member

December 20, 2003
Blacksburg, Virginia

Keywords: Gyrostat, Internal Torques, Active Magnetic Bearings, Spacecraft Simulator

Abstract

Internal Torques and Forces in Gyrostats with Magnetically Suspended Rotors

Marcus Carl Pressl

Active magnetic bearings have several potential applications in spacecraft design. Based on the gyrostat model, we develop equations that describe the internal torques and forces that occur between the body and one of the attached wheels. We evaluate the transverse torques for the torque–free gyrostat and a gyrostat undergoing attitude maneuvers using momentum wheels and external torques. We then apply these internal forces to a model of an active magnetic bearing system and discuss their effects on the force limit, the actuator slew rate and the equivalent stiffness and damping parameters. As a basis for this study we use the Distributed Spacecraft Attitude Control System Simulator (DSACSS) with a Revolve MBRotor active magnetic bearing system. The results of several numerical simulations show that the magnitude and frequency of the internal torques remain small over the estimated range of motion of the DSACSS–MBRotor gyrostat. As such, the transverse torques caused by the rotational motion remain less than the discussed performance limits. We show that the magnitude of the internal torques can also be minimized by reducing the axial moment of inertia of the wheel. Furthermore, we discuss the equivalent Jeffcott model. By applying a standard Proportional–Integral–Derivative controller to the active magnetic bearing both the equivalent stiffness and damping parameters remain constant.

Contents

List of Figures

List of Tables

Chapter 1

Introduction

Applications for active magnetic bearings in spacecraft have been discussed since the early days of the space program. Magnetic bearings have been used successfully to support reaction wheels in several European satellites in the SPOT series. Other applications, such as flywheels, are now becoming feasible due to magnetic bearing technology. Flywheels store rotational energy and are a possible alternative to chemical batteries. However, they require bearings with minimal friction levels, which only magnetic bearings can provide.

Magnetic bearings also have the potential of being used as rate sensors. The net force generated in the bearings is a function of the rotors' position and the applied current. The position is the measured state and the current is the output of a feedback control system. Both quantities are therefore readily available during the bearing's operation. As a result, the net force is also a known quantity. The forces caused by the rotational motion of the spacecraft can therefore be measured using the sensors which are an inherent part of active magnetic bearings. Since these forces are proportional to the angular velocities of spacecraft, it is possible to use these measurements to determine these angular velocities.

The most common type of bearings used in spacecraft today are anti–friction bearings. Despite their name, anti–friction bearings still have substantial frictional losses. These losses require larger actuator motors and power sources, which increase the weight and cost of the spacecraft. The term "anti–friction bearing" refers to the type of bearing which relies on rolling elements, as opposed to fluid films. These bearings come in a variety of designs. Each design has an outer ring, or race, mounted to a structure, and an inner race attached to

the shaft of the rotating machinery. Between the rings are the rolling elements. Depending on the design these elements can be either cylindrical or spherical, as in the well–known ball bearings. In some cases, the outer race is shaped such that the rolling elements have a tapered or spherical arrangement. Anti–friction bearings have a limited lifetime, which is determined by a purely statistical method. It is therefore impossible to predict when a given bearing will fail. Causes of failures include improper installation, dirt, lack of lubrication and manufacturing defects.

Active Magnetic Bearing systems provide several advantages over conventional bearings. By relying on magnetic suspension, there is no physical contact between the rotor and the stator. The rotor, sometimes called the target, is the rotating machinery suspended in the magnetic field. Depending on the application, the rotor can be an energy storing flywheel or simply a momentum wheel. The term stator refers to the electromagnetic poles that surround the rotor. These poles generate the attractive magnetic force, which keeps the rotor suspended. The stator is equivalent to the outer race of the anti–friction bearings. The lack of contact between the rotor and the stator reduces friction and the need for lubrication.

Another advantage of magnetic bearing technology is that the wear of all the mechanical components is reduced, which leads to an increase in the lifetime of the bearing. Since magnetic bearings contain shaft position and coil current sensors as elements of their control system, they provide inherent diagnostic abilities that are absent in most other bearing types. These control systems also provide levels of vibration control that conventional bearings do not have.

One of the disadvantages of magnetic bearings is the need for a power source. Depending on the size of the bearing system, the power requirements can be quite large. For smaller systems, such as momentum actuators, these power requirements may not become a limiting factor. Furthermore, magnetic bearings are more expensive than their conventional counterparts. The higher cost is due to the additional hardware that is required to operate magnetic bearings. In most cases, the initial expenses are recovered in the savings received from lower maintenance and repair costs.

The subject of this thesis is the internal forces on momentum or flywheels that are mounted in a rotating spacecraft. The internal forces are generated by the rotational maneuvers of the spacecraft, also called the platform. These forces can potentially affect the performance of a magnetic bearing system. In addition, larger bearing loads require more power, therefore

increasing the weight and cost of the spacecraft. Knowing the magnitude of these forces allows the proper sizing of the magnetic bearings during the design phase.

In the near future, The Space Systems Simulation Laboratory at Virginia Tech will perform magnetic bearing base motion experiments. The Distributed Spacecraft Attitude Control System Simulator (DSACSS), otherwise referred to as Whorl–1, will serve as the rotating platform to a Revolve MBRotor magnetic bearing system. We use this experimental setup as the spacecraft model for this thesis. However, we make the assumption that Whorl–1 is a freely rotating rigid body and therefore place no limits on its possible motion. A detailed description of both Whorl–1 and the MBRotor kit is included in the Appendices A and B, respectively. This setup is best described by the dynamical model of a gyrostat. We introduce the equations of motion of a gyrostat and discuss an analytical as well as a numerical solution. Based on the gyrostat model, we develop equations for the internal transverse torques on one of the wheels in a n-wheel gyrostat. To study the transverse torques, we consider three separate cases. We explore a gyrostat without external or axial wheel torques, followed by a gyrostat undergoing attitude maneuvers. The third case investigates the effects of external torques on the gyrostat. We introduce a magnetic bearing theory and evaluate the impact of the transverse torques on the magnetic bearing performance. Specifically, we consider the peak force limit, the actuator slew rate and the equivalent stiffness and damping values of the radial magnetic bearings.

Chapter 2

Literature Review

In this chapter we give a review of the literature that is related to the use of active magnetic bearings subject to base motion. This area is relatively new and there are few publications which specifically address this topic. Therefore, we also include several publications that begin with more fundamental topics that will be useful later in the development of the equations of the dynamics. We begin with the literature on gyrostat dynamics and the fundamentals of magnetic bearing theory. We then discuss publications on performance limits of magnetic bearings and conclude with a discussion on the current literature on other types of base motion studies as well as studies on magnetic bearings for space applications.

2.1 Gyrostats

For the most part, papers on performance analysis of bearing systems fall into the field of rotor dynamics. Such is also the case for active magnetic bearings (AMB) systems. These bearing systems are commonly mounted on strong concrete foundations to avoid any excitation due to base motion. This setup allows the rotor dynamics model to be based on a mass-spring-damper system. However, we are assuming that the magnetic bearing will be part of a spacecraft or spacecraft simulator. The platform on which the bearing is mounted will undergo large rotational maneuvers at different angular velocities. This motion will create forces in the magnetic bearing.

A gyrostats represent a well–studied model in rigid body dynamics. It consists of an assembly

of a rigid body and a rotor that is free to spin about a fixed axis, relative to the body. This model is fundamental to many attitude dynamics and control problems for spacecraft and is ideal for the study of magnetic bearings undergoing base motion. The dynamics of gyrostats have been the subject of many publications over the last two centuries. Good introductions to the gyrostat equations of motion were given by Leimanis[1] and Hughes.[2] Leimanis' main focus was on the development of the analytical solution to the equations of motion, which can be expressed in terms of elliptic functions. A similar treatment of the gyrostat closed–form solution can be found in the work by Wittenburg.[3] Hall and Rand[4] also contributed to this discussion with their study of the spin-up dynamics of gyrostats. Hughes developed the gyrostat model and continued to expand on it in the context of the spacecraft attitude control problem. None of these texts specifically focus on transverse torques that occur between the base body and the rotor, but provide the framework needed to derive them.

2.2 Magnetic Bearing Theory

Compared to gyrostats, magnetic bearing technology is a relatively new research area, even though the physics of magnetic circuits have been known. A good introduction to the underlying physics of electromagnetism can be found in Plonus.[5] Although Plonus does not address magnetic bearings specifically, topics such as magnetic circuits and saturation are explained thoroughly.

Allaire *et al*[6,7] discussed the fundamental theory of active magnetic bearing systems. The first article described the design of a low power magnetic bearing system including basic control theory. Like the majority of earlier publications, Allaire described the use of a Proportional-Integral-Derivative (PID) controller*. The second article by Allaire *et al*[7] gave a detailed derivation of the equation representing the force in the air gap of electromagnets. This article also presented a design example of a motor pump for petrochemical industrial plants. The sections on the control theory presented a more detailed discussion and included the effects of the position sensors and the power amplifier in the final transfer function. Both articles introduced the linearization of the force equation that demonstrates the inherent instability of the open loop magnetic circuit due to the fact that the open loop stiffness is always negative. Like all other bearing types, magnetic bearings have limitations that have been discussed in several articles for various different applications. One of the earlier discus-

*Recently, different types of controllers have been proposed for active magnetic bearings but are not discussed in this thesis.

sions of magnetic bearing performance limits was given by Maslen *et al*.[8] They presented equations for the saturation force limit, the force slew rate limits, and the displacement sensitivity. The authors also demonstrated the effects of those limitations with an experimental magnetic bearing test bed. In addition, the paper gave generic guidelines of how these performance limits can be used in the design of active magnetic bearings.

Based on Maslen's work, Bornstein[9] investigated the limits of magnetic bearings undergoing dynamic loads. He introduced the two classifications of Class-A and Class-B controls. Class-A refers to bearings using two opposing electromagnetic actuators, whereas Class-B controllers rely on only one actuator. Bornstein presented equations that outline the dynamic capabilities for both types of bearing designs, and concluded that Class-A bearings have a higher maximum dynamic load which is independent of the static load. Siegwart and Traxler[10] analyzed the performance limits of an active magnetic bearing system of a milling spindle and derived an expression for the dynamic loading capabilities similar to Bornstein's.

Rao *et al*[11] included static loads in their analysis of the stiffness of magnetic bearings undergoing dynamic loads. In their paper, the authors demonstrated that the ratio of dynamic and static loads influences the bearing stiffness. Based on a survey of reported bearing tests they estimated the usable gap fraction necessary for supporting dynamic loads.

Even though most of the work we present here is based on numerical simulations, it is important that we test the results based on a meaningful magnetic bearing model. We therefore choose to apply the analysis to the MBRotorKit manufactured by Revolve. The bearing specifications can be found in the MBRotor manual.[12] Additional information on the internal controller and power amplifier are included in the manual for the MB350 module.[13] As a moving platform, we use the Distributed Spacecraft Attitude Control System Simulator (DSACSS), otherwise known as Whorl-1, which is described by Schwartz *et al*[14] [†].

2.3 Base Motion Studies

The idea of using active magnetic bearings in spacecraft has been suggested quite frequently, but few actual studies have been published. In fact, few papers address the performance of magnetic bearings undergoing base motion. In his recent Master's thesis, Clements[15]

[†]Details on the ongoing developments of the DSACSS project can be found at: http://www.aoe.vt.edu/research/groups/sssl.

performed a simple base motion study of a magnetic bearing system mounted on a shaker table. This shaker table produced sinusoidal excitation frequencies up to 27 Hz. Clements compared the results from the experiment with results predicted from a model. His work in regards to characterization of the magnetic bearing and its components is helpful since he used the same version of the Revolve^{TM}MBRotor kit that is the basis of the model for this paper.

Even though this and similar investigations are helpful in the study of magnetic bearing systems in vehicles such as cars or ships, they do not include the effects due to rotational maneuvers as seen by spacecraft or aircraft. Several papers published within the European space community, ESA and various aerospace related corporations, have discussed magnetic bearing systems. Some of them even describe tests of magnetic bearing systems mounted on air bearing platforms. These tests are similar to those underway at Virginia Tech. Robinson,[16] for example, described the advances of using magnetically suspended momentum wheels for spacecraft attitude control. He explained the various configurations of momentum wheels with up to 5 degrees of freedom. In addition, he discussed several examples of these configurations that were designed by Teldix and British Aerospace companies. In a similar article, Robinson[17] outlined the design of a prototype reaction wheel using magnetic bearings. More recent studies on these topics can be found in Scharfe *et al*[18],.[19] In these articles, the authors outlined the design and implementation of momentum wheels for the AMSAT Phase 3-D and the PROBA satellites.

The French SPOT satellite launched in February of 1986, was the first satellite to use magnetic bearing reaction wheels. Since then, ESA has launched several other satellites in the SPOT family and others that employed this technology successfully.

Having presented several publications that form the background to the study we present in this thesis, we now turn to developling the necessary equations of motion of the gyrostat model. These equations provide the foundation from which we derive expressions for the transverse torques acting on a wheel in a gyrostat.

Chapter 3

Gyrostat Model

The analysis of forces inside of bearings is frequently performed and described in sufficient detail in literature about rotor dynamics. In the majority of cases, the bearing system is stationary or, at most, subjected to an oscillatory base motion. Since we are interested in evaluating the performance of magnetic bearing systems used for spacecraft momentum wheels, these models are not appropriate. A magnetically suspended momentum wheel will undergo motions that are better described by rigid body dynamics. In this chapter, we introduce the dynamical model of a gyrostat and develop its equations of motion. From these equations, we derive expressions that relate the rotational motion to the forces that are developed inside the magnetic bearings.

3.1 Equations of Motion

A gyrostat is a mechanical system that consists of at least two rigid bodies, the first of which we call platform P. Connected to this platform are the remaining rigid bodies which we call the wheels R_i, where $i = 1, \cdots, n$. Each wheel is inertially axisymmetric and spins about a fixed axis $\vec{a}_i$ with respect to the platform. This general description can be applied to many systems. In fact, Leimanis[1] began his discussion of gyrostats with the example of a propeller aircraft flying under the influence of aerodynamic forces. Hughes,[2] on the other hand, applied this model to satellites that use wheels as attitude control actuators. Here, we are interested in the effects of rotational motion on wheels mounted on a spacecraft

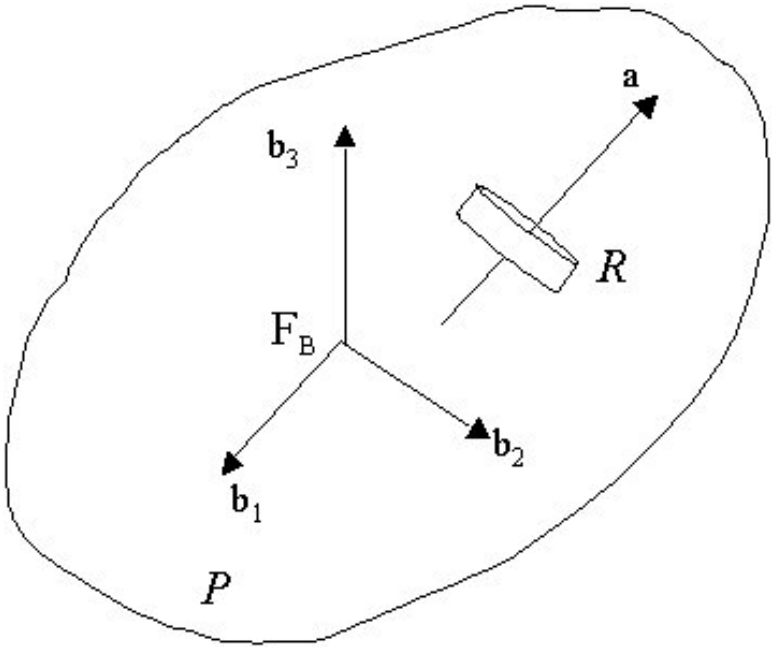

Figure 3.1: *Gyrostat Model with One Rotor*

simulator.

Two common types of rotor actuators used in space applications are reaction wheels and momentum wheels. Both affect the total body angular momentum of the system by changing the rotational speed of the rotor. Whereas reaction wheels have a nominal zero spin rate, momentum wheels have a given non–zero spin rate. A motor is used to produce an axial torque g_a on these rotors which causes a change in the spin rate. The simplest model of a spacecraft with momentum wheels is called a gyrostat. The equations of motion of the gyrostat model have been studied extensively and can be found in several textbooks on classical dynamics. Besides the references by Leimanis[1] and Hughes,[2] additional information can be found in Wittenburg[3] and Hall *et al.*[4]

A generalized gyrostat model is shown in Figure 3.1. For the general case, the gyrostat can contain up to n wheels. First, we define a body-fixed coordinate frame $\mathcal{F}_B$, with the base vectors $\hat{b}_1$, $\hat{b}_2$ and $\hat{b}_3$. Without loss of generality, we assume that $\mathcal{F}_B$ is the frame that diagonalizes the inertia matrix $\mathbf{I}$. The inertia matrix $\mathbf{I}$ represents the total inertia of the system $P + \sum_{i=1}^{n} R_i$ and is expressed in $\mathcal{F}_B$. We also define a diagonal inertia matrix $\mathbf{I}_s$ that contains the axial moments of inertia of the wheels. Furthermore we collect all spin

axis vectors in a $3 \times n$ matrix $\mathbf{A}$ such that $\mathbf{A} = [\mathbf{a}_1 \dots \mathbf{a}_n]$. Finally, we define the inertia-like matrix $\mathbf{J} = \mathbf{I} - \mathbf{A}\mathbf{I}_s\mathbf{A}^T$. The diagonal 3×3 matrix $\mathbf{J}$ represents the gyrostat's moments of inertia without the contribution of the axial wheel inertia. With these definitions we can formulate the equations of motion for the gyrostat model. The angular momentum of the system, expressed in $\mathcal{F}_B$ is given by:

$$\mathbf{h} = \mathbf{I}\omega + \mathbf{A}\mathbf{I}_s\omega_s \tag{3.1}$$

Here, ω is the angular velocity of $\mathcal{F}_B$ with respect to inertial space, and ω_s is an $n \times 1$ column matrix containing the axial angular velocities of the n rotors with respect to $\mathcal{F}_B$. The total angular momentum of equation (3.1) is therefore the sum of the angular momentum of the gyrostat and the contribution of the rotor spins along the respective axes of rotation. Similarly, we define the axial angular momenta $\mathbf{h}_a$ of the rotors with respect to inertial space:

$$\mathbf{h}_a = \mathbf{I}_s\mathbf{A}^T\omega + \mathbf{I}_s\omega_s \tag{3.2}$$

The rotational equations of motion for the gyrostat, again expressed in $\mathcal{F}_B$, can therefore be written as:

$$\dot{\mathbf{h}} = \mathbf{h}^\times\omega + \mathbf{g}_e \tag{3.3}$$

$$\dot{\mathbf{h}}_a = \mathbf{g}_a \tag{3.4}$$

The column matrix $\mathbf{g}_e$ is the 3×1 vector of the external torques applied to the system. In general, $\mathbf{g}_e$ depends on the environment in which the gyrostat is to be analyzed. If we are modeling a spacecraft, $\mathbf{g}_e$ will include terms such as gravity gradient, solar pressure and thruster torques. The "×" symbol refers to the skew-symmetric operator which is the matrix equivalent to a vector cross–product. The skew–symmetrix operator is defined by the following expression:

$$\mathbf{a}^\times = \begin{bmatrix} 0 & -a_3 & a_2 \\ a_3 & 0 & -a_1 \\ -a_2 & a_1 & 0 \end{bmatrix} \tag{3.5}$$

The axial torques, which are the result of motors acting on each of the rotors respectively, are collected in the $n \times 1$ matrix $\mathbf{g}_a$. By combining equations (3.1) and (3.2), we can express the angular velocity of $\mathcal{F}_B$ as:

$$\omega = \mathbf{J}^{-1}(\mathbf{h} - \mathbf{A}\mathbf{h}_a) \tag{3.6}$$

With this definition we can rewrite equation (3.3) to express $\dot{\mathbf{h}}$ as:

$$\dot{\mathbf{h}} = \mathbf{h}^\times\mathbf{J}^{-1}(\mathbf{h} - \mathbf{A}\mathbf{h}_\mathbf{a}) + \mathbf{g}_\mathbf{e} \tag{3.7}$$

To provide meaning to this analysis, it is usually beneficial to simulate an actual spacecraft. In this case, the basis for our model is the Distributed Spacecraft Attitude Control System Simulator (DSACSS), otherwise referred to as Whorl–1, operated at Virginia Tech. A detailed description of Whorl–1 is included in Appendix A. To define the body–fixed reference frame $\mathcal{F}_{\mathcal{B}}$, we choose Whorl-1's major axis to lie in the $\hat{b}_3$ direction, so that the $\hat{b}_1$ and $\hat{b}_2$ vectors lie in a plane parallel to the lower deck of Whorl-1. Since Whorl-1 is not homogeneous, the moments of inertia in the $\hat{b}_1$ and the $\hat{b}_2$ directions are not equal. In fact, I_2 is slightly larger than I_1. By choice, we align the rotor's spin axis parallel to the $\hat{b}_1$ axis. A CAD model provides estimates for the inertia parameters. These estimates, which are used throughout this analysis, are :

$$\mathbf{I} = \begin{bmatrix} 7.47 & 0 & 0 \\ 0 & 8.51 & 0 \\ 0 & 0 & 11.73 \end{bmatrix} \quad [\text{kg m}^2] \tag{3.8}$$

The actual inertia parameters are not yet known. In the near future, experimental methods will be implemented to establish the exact values. Even though we assume here, that the rotor is aligned with the $\hat{b}_1$ axis, this is unlikely. However, with this preliminary information, we are still able to develop a generalized model and draw conclusions from the simulations.

Based on the choice of reference frame, we can arrange the moments of inertia of the $P + R$ system as $I_3 > I_2 > I_1$. In reference [4] the authors identify three general types of gyrostat systems based on the relative magnitude of the three principal inertia parameters.

$$\text{gyrostat model is} \begin{cases} \textbf{oblate} \text{ if } I_P > I_2 > I_3 \\ \textbf{prolate} \text{ if } I_3 > I_2 > I_P \\ \textbf{intermediate} \text{ if } I_3 > I_P > I_2 \end{cases}$$

Here, I_P represents the moment of inertia of only the platform P about the B_1 axis and is equal to J_1 or $I_P = I_1 - I_P$. We can therefore see that the proposed gyrostat model is prolate. This insight will be of importance when we consider the analytical solution to the equations of motion. Applying equations (3.3) and (3.4) to this one-rotor model gives the

following equations of motion written in scalar form:

$$\dot{h}_1 = \frac{I_2 - I_3}{I_2 I_3} h_2 h_3 \tag{3.9}$$

$$\dot{h}_2 = \left(\frac{I_3 - I_P}{I_3 I_P} h_1 - \frac{h_a}{I_P} \right) h_3 \tag{3.10}$$

$$\dot{h}_3 = \left(\frac{I_P - I_2}{I_2 I_P} h_1 + \frac{h_a}{I_P} \right) h_2 \tag{3.11}$$

$$\dot{h}_a = g_a \tag{3.12}$$

Equations (3.9) through (3.12) form the basis for the following analysis.

There are several methods to solve these equations of motion. The two most common approaches are numerical simulation or the development of an analytical solution. In classical dynamics, analytical solutions are preferred. However, currently we only have analytical expressions for torque–free gyrostats. To include either external or axial control torques, we resort to numerical simulations of the equations of motion. With the exponential increase in the capabilities of modern computers, computational errors introduced by the numerical solutions are sufficiently small. Simulations are therefore acceptable for most engineering applications. We discuss both an analytical and a numerical solution to the equations of motion of the gyrostat.

3.2 An Analytical Solution

In this section we focus on deriving analytical solutions to the gyrostat equations of motion. Due to the nonlinear characteristics of these equations, analytical solutions can only be found for specific limited cases. For the following discussion, we make the limiting assumption that $g_{ex} = g_a = 0$, *i.e.* that no external nor axial torques are acting on the platform and the rotor respectively. Therefore, the angular momentum of the $P + R$ system remains constant. Since this assumption parallels Section 4.2, we can directly apply the resulting dynamical equations to solve for the transverse torques in equations (4.11) through (4.13).

The method of finding the analytical solution for the motion of a gyrostat has been studied extensively. In many ways, it is identical to the analysis of a single rotating rigid body. The derivation presented here, follows the approach used by both Leimanis[1] and Wittenburg.[3] We begin by revisiting equations (3.9) through (3.11), expressed as functions of the angular

velocity of the gyrostat.

$$\dot{\omega}_1 = \frac{I_2 - I_3}{I_P}\omega_2\omega_3 \tag{3.13}$$

$$\dot{\omega}_2 = \frac{I_3 - I_1}{I_2}\omega_3\omega_1 - \frac{I_s}{I_2}\omega_3\omega_s \tag{3.14}$$

$$\dot{\omega}_3 = \frac{I_1 - I_2}{I_3}\omega_1\omega_2 + \frac{I_s}{I_3}\omega_2\omega_s \tag{3.15}$$

To arrive at this set of equations, we also make the assumption that $\omega_s = const$*. We note that h_a therefore is not constant. By inspection, we see that the Hamiltonian of the gyrostat is simply its rotational kinetic energy. Since we are interested in the torque–free case the Hamiltonian remains constant. We define an energy–based constant c_1, which can be written as:

$$c_1 = 2T = I_P\omega_1^2 + I_2\omega_2^2 + I_3\omega_3^2 \tag{3.16}$$

Similarly, we find that the magnitude of the angular momentum of the gyrostat remains constant:

$$h^2 = I_P^2\omega_1^2 + I_2^2\omega_2^2 + I_3^2\omega_3^2 + 2I_P\omega_1 h_a + h_a^2 \tag{3.17}$$

For simplification, we define the quantitiy $c_2 = h^2 - h_a^2$, so that (3.17) becomes:

$$c_2 = I_P^2\omega_1^2 + I_2^2\omega_2^2 + I_3^2\omega_3^2 + 2I_P\omega_1 h_a \tag{3.18}$$

These two equations, (3.16) and (3.18), are referred to as the two integrals of motion. A derivation of these two equations can be found in Leimanis.[1] Using these two equations, we express $\dot{\omega}_1$ solely as a function of ω_1. First, we find an expression for ω_2 in terms of ω_1 by multiplying equation (3.16) by I_3 and subtracting the result from equation (3.17). Similarly we subtract equation (3.16), multiplied by I_2, from (3.17) and find an expression of ω_3 in terms of ω_1. The resuliting expressions for ω_2 and ω_3 are:

$$\omega_2 = \sqrt{\frac{I_p(I_3 - I_P)}{I_2(I_2 - I_3)}P_y}, \qquad P_y = \omega_1^2 - \left(\frac{2h_a}{I_3 - I_P}\right)\omega_1 + \frac{c_2 - I_3 c_1}{I_3 - I_P} \tag{3.19}$$

$$\omega_3 = \sqrt{\frac{I_P(I_2 - I_P)}{I_3(I_3 - I_2)}P_z}, \qquad P_z = \omega_1^2 - \left(\frac{2h_a}{I_2 - I_P}\right)\omega_1 + \frac{c_2 - I_2 c_1}{I_P(I_2 - I_P)} \tag{3.20}$$

Substituting these two expressions into $\dot{\omega}_1$ we find:

$$\dot{\omega}_1 = \sqrt{\frac{(I_3 - I_P)(I_2 - I_P)}{I_2 I_3}}\, i\sqrt{P_y P_z} \tag{3.21}$$

* Commonly referred to as Kelvin's gyrostat.[2] The other case, where $h_a = 0$, is called the apparent gyrostat.

Leimanis refers to the expression $W = P_y P_z$ as the gyroscopic function. The solution to the gyroscopic function is found using the following integral:

$$t = \int_{\omega_1(0)}^{\omega_1} \frac{d\omega_1}{i\sqrt{W}} \tag{3.22}$$

The result of this integration gives an expression for the time t as a function of ω_1, or by inversion, $\omega_1(t)$. Since the gyroscopic function is a product of two quadratic polynomials in ω_1, the result is a quartic polynomial. The integral from equation (3.22) can therefore be expressed in terms of the roots of the gyroscopic function:

$$t = \int_{\omega_1(0)}^{\omega_1} \frac{d\omega_1}{\sqrt{-(\omega_1 - a)(\omega_1 - b)(\omega_1 - c)(\omega_1 - d)}} \tag{3.23}$$

There are several possibilities for the solution of the integral in equation (3.23). The roots of W can be real, complex or one of five other combinations thereof. The combination of roots determines which kind of solution can be found. For valid, non–stationary solutions, only two combinations are possible: combinations in which all four roots are real, or combinations which have two real roots and a complex conjugate pair. Both Hall[4] and Leimanis[1] discuss the various solutions in depth. Without imposing too many restrictions, we focus only on the first case, in which all four roots to the gyroscopic function are real. This case also corresponds to the solution based on a prolate gyrostat model, where $I_3 > I_2 > I_1$. We find that the integral in equation (3.23) is equivalent to equation 256.00 in Byrd and Friedman[20] and can therefore be solved as an elliptic integral. Expressing ω_1 as a function of time we find:

$$\omega_1(t) = b\left(\frac{1 - c\alpha_1^2 \mathrm{sn}^2(u;k)}{1 - \alpha^2 \mathrm{sn}^2(u;k)}\right) \tag{3.24}$$

To arrive at equation (3.24), the roots of W are ordered such that $a \geq \omega_1 \geq b > c > d$. The constants α^2, α_1^2 are defined as:

$$\begin{aligned} \alpha^2 &= \frac{a-b}{a-c} \\ \alpha_1^2 &= \frac{c}{b}\alpha^2 \end{aligned}$$

The argument u and the modulus k are given by:

$$\begin{aligned} u &= \frac{2t}{\sqrt{\frac{(I_3 - I_p)(I_2 - I_p)(-P_y)P_z}{I_2 I_3}}} \\ k &= \frac{(a-b)(c-d)}{(a-c)(b-d)} \end{aligned}$$

Having found the function $\omega_1(t)$ we can then determine $\omega_2(t)$ and $\omega_3(t)$. These two expressions are given by:

$$\omega_2(t) = \sqrt{\frac{(a-b)(b-d)I_p(I_3-I_p)}{I_2(I_2-I_3)}}\,\frac{\mathrm{cn}(u;k)\mathrm{dn}(u;k)}{1-\alpha^2\mathrm{sn}^2(u;k)} \tag{3.25}$$

$$\omega_3(t) = \sqrt{\frac{\alpha^2 I_p(I_2-I_p)}{(I_3-I_2)I_3}}\,\frac{(b-c)\mathrm{sn}(u;k)}{1-\alpha^2\mathrm{sn}^2(u;k)} \tag{3.26}$$

Both equations (3.25) and (3.26) together with (3.24) represent the exact solution of the gyrostat equations of motion. Given a set of inertia parameters and initial angular velocity values, the motion of the system can be determined.

3.3 Numerical Solution

Even though an exact solution is always more desirable, it is often difficult to find. For gyrostats, the method for finding the exact solution depends on the initial conditions. By slightly changing the moments of inertia or the initial angular velocity vector, the roots of the gyroscopic function will change enough such that the functions for $\omega_1(t)$, $\omega_2(t)$ and $\omega_3(t)$ found in the previous section will no longer be valid. Even though it is possible to write a program that will identify all seven possible cases and select between the four solution methods outlined in Leimanis,[1] it is just as efficient to numerically integrate the equations of motion directly. With this approach, we can find solutions to the gyrostat motion that are not limited by previous assumptions *i.e.* no axial or external torques. The results presented in this paper are the product of several Matlab simulations. Similar results of gyrostat simulations were reproduced with programs in C++, the latter making use of the OPEN SESSAME[21] framework. The numerical approach can be partitioned into 3 steps:

1. Solving the equations of motion for the gyrostat
2. Calculating the transverse torques and bearing reaction forces
3. Determining the relative error

The first step requires the straightforward integration of equations (3.3) and (3.4). Once the angular momentum of the gyrostat is known for a given time span, equation (3.6) can

be used to calculate the angular velocities, and equations (3.13)–(3.15) to find the time derivatives of the angular velocities. The transverse torques and the reaction forces are then calculated. The equations for the torques and forces are introduced in the Chapter 4. To determine if the calculated torques are actually correct, we treat the rotor itself as a rotating rigid body and use Euler's rotational equations to determine its motion. Here, we use the transverse torques, the given axial and external torques as inputs and then solve for the angular velocities of this rotor equivalent rigid body. Finally, we compare the resulting angular velocities of the rotor found by integrating Euler's equations with those determined by the actual gyrostat integration. To integrate these equations of motion, we use a 4th order Runge–Kutta integrator. The states for both the gyrostat and the rotor equivalent rigid body are contained in the same state vector. Using global variables, the transverse torques, which are determined during the integration, are stored and can be evaluated after the integration is complete.

The difference between the angular velocities that result from the motion of the rotor as mounted on the gyrostat platform and the angular velocities of a rotor treated as a rigid body moving under the influence of the transverse torques gives an indication of the accuracy of the numerical simulation. In general the relative error of ω_2 and ω_3 is on the order of 10^{-16} and the relative error for ω_1 is slightly larger with magnitudes on the order of 10^{-14}. These relative errors are within the precision set for the numerical simulations.

In this chapter, we introduced and developed the gyrostat model. The equations of motion of the gyrostat are well–known, and we apply these equations to the Whorl–1 spacecraft simulator. Both an analytical and numerical solution were presented.

Chapter 4

Transverse Torques

Having solved the equations of motion of the gyrostat, we can now focus on the effects of its motion on the rotor. As the gyrostat rotates, bearings will provide support to the rotor. The torques caused by the rotational motion of the platform are due to to forces between the rotor and the stator inside the bearings. Currently most momentum wheels use anti–friction bearings, in which the rotor and the stator are in direct contact. In active magnetic bearings, the rotor and the stator interact via a magnetic field. The strength of the magnetic field is subject to several performance limits. Therefore, we seek an expression, describing the torques that occur between the rotor and platform. In this chapter, we derive an equation for the transverse torques and study the effects of the platform's motion and the rotor's inertia parameters.

4.1 Deriving the Transverse Torque Equations

To study the effects of transverse torques acting on a rotor in a gyrostat, we treat the rotor as a rigid body by itself. The equations describing rigid body rotational motion are the well–known Euler's equations. Expressing these equations in matrix form in a body–fixed frame, we have:

$$\mathbf{I}_r\dot{\boldsymbol{\omega}}_r = -\boldsymbol{\omega}^{\times}\mathbf{I}_r\boldsymbol{\omega}_{\boldsymbol{r}} + \mathbf{g}_r \tag{4.1}$$

In equation (4.1), the principal moments of inertia of the rotor are contained in $\mathbf{I}_r$. The vector $\mathbf{g}_r$ represents the torques acting on the rotor. We also distinguish between the angular

velocity $\boldsymbol{\omega}_r$ of the rotor and the angular velocity $\boldsymbol{\omega}$ of the body fixed reference frame. Since we prefer to have all quantities expressed in the same frame, we use the reference frame $\mathcal{F}_B$, which is fixed in the gyrostat rather than in the rotor. This is only possible because the rotor is symmetric about its spin axis $\mathbf{a}$. Even while the rotor is spinning relative to the platform, the gyrostat's inertia matrix remains constant. By choice, $\mathcal{F}_B$ therefore becomes a nodal frame for the rotor. The difference between $\boldsymbol{\omega}_r$ and $\boldsymbol{\omega}$ then becomes the relative spin ω_s. In general, we can write $\boldsymbol{\omega}_r$ for a rotor spinning about an axis $\mathbf{a}$:

$$\boldsymbol{\omega}_r = \boldsymbol{\omega} + \mathbf{a}\omega_s \tag{4.2}$$

The time derivative of equation (4.2) is:

$$\dot{\boldsymbol{\omega}}_r = \dot{\boldsymbol{\omega}} + \mathbf{a}\dot{\omega}_s \tag{4.3}$$

Rearranging equation (4.1), we find the torques $\mathbf{g}_r$ acting on the rotor:

$$\mathbf{g}_r = \mathbf{I}_r\big(\dot{\boldsymbol{\omega}} + \mathbf{a}\dot{\omega}_s\big) + \boldsymbol{\omega}^{\times}\mathbf{I}_r\big(\boldsymbol{\omega} + \mathbf{a}\omega_s\big) \tag{4.4}$$

The value of the scalar $\dot{\omega}_s$ can be found by taking the time derivative of equation (3.2). The matrix $\mathbf{A}$ is replaced by the column matrix $\mathbf{a}$ which represents the spin axis of the rotor of interest. Noting that $\dot{h}_a = g_a$ we can express $\dot{\omega}_s$ as:

$$\dot{\omega}_s = \frac{g_{ar}}{I_s} - \mathbf{a}^T\dot{\boldsymbol{\omega}} \tag{4.5}$$

The axial torque g_{ar} is the particular component of the $\mathbf{g}_a$, acting on the rotor of interest. Substituting equation (4.5) into equation (4.4) and simplifying gives:

$$\mathbf{g}_r = \mathbf{I}_r\left[(\mathbf{1} - \mathbf{a}\mathbf{a}^T)\dot{\boldsymbol{\omega}} + \mathbf{a}\frac{g_{ar}}{I_s}\right] + \boldsymbol{\omega}^{\times}\mathbf{I}_r(\boldsymbol{\omega} + \mathbf{a}\omega_s) \tag{4.6}$$

Here the symbol $\mathbf{1}$ represents the 3×3 identity matrix, and $\mathbf{a}\mathbf{a}^T$ is the matrix representation of the dyadic $\vec{a}\vec{a}$. To solve equation (4.6) we need to know the time rate of change of the angular velocity of $\mathcal{F}_B$, which is the same as that of the gyrostat. Taking the time derivative of equation (3.1) we find:

$$\dot{\mathbf{h}} = \mathbf{I}\dot{\boldsymbol{\omega}} + \mathbf{A}\mathbf{I}_s\dot{\boldsymbol{\omega}}_s \tag{4.7}$$

Here, we need an expression for the time rate of change of the relative rotor spin rate. In the general case, the gyrostat has multiple rotors. Following the notation from Section 3.1 we differentiate equation (3.2) with respect to time and solve for $\dot{\boldsymbol{\omega}}_s$:

$$\dot{\boldsymbol{\omega}}_s = \mathbf{I}_s^{-1}\left[\mathbf{g}_a - \mathbf{I}_s\mathbf{A}^T\dot{\boldsymbol{\omega}}\right] \tag{4.8}$$

Substituting this expression into (4.7) we can rewrite this equation as:

$$\dot{\mathbf{h}} = \Big[\mathbf{I} - \mathbf{A}\mathbf{I}_s\mathbf{A}^T\Big]\dot{\boldsymbol{\omega}} + \mathbf{A}\mathbf{g}_a \tag{4.9}$$

Here, we recognize the inertia–like parameter $\mathbf{J} = \mathbf{I} - \mathbf{A}\mathbf{I}_s\mathbf{A}^T$ that was introduced in Section 3.1. The final step is to replace $\dot{\mathbf{h}}$ in equation (3.3) with (4.9) and solve for $\dot{\boldsymbol{\omega}}$:

$$\dot{\boldsymbol{\omega}} = \mathbf{J}^{-1}\Big[\mathbf{g}_e - \boldsymbol{\omega}^{\times}\mathbf{h} - \mathbf{A}\mathbf{g}_a\Big] \tag{4.10}$$

We note that this expression for the time rate of change of the angular velocities of the gyrostat is valid regardless of the nature of the external torques or axial rotor torques. Equations (4.6) and (4.10) allow us to solve for the torques acting on the rotor for any controlled or uncontrolled motion of the gyrostat. With the formulation developed here and and the equations of motion presented in Section 3.1, we can model n-rotor gyrostats. We can therefore study the effects of the torques on rotors that are being used as momentum exchange devices or rotors that are intended as energy–storing flywheels.

One specific case occurs, when the rotor is mounted parallel to one of the principal axes of the gyrostat. Based on the Whorl–1 model we explore the case where the rotor of interest is aligned with the $\hat{b}_1$ axis. This assumption reduces equation (4.6) to the following equations in component form:

$$g_{r1} = g_{ar} \tag{4.11}$$

$$g_{r2} = I_t\dot{\omega}_2 + \omega_1\omega_3\big(I_s - I_t\big) + I_s\omega_s\omega_3 \tag{4.12}$$

$$g_{r3} = I_t\dot{\omega}_3 + \omega_1\omega_2\big(I_t - I_s\big) - I_s\omega_s\omega_2 \tag{4.13}$$

We observe from this set of equations that the transverse and axial torques are decoupled. This observation remains true as long as the rotor is aligned with one of the axes of $\mathcal{F}_B$. In this case, the term $(\mathbf{1} - \mathbf{a}\mathbf{a}^T)\dot{\boldsymbol{\omega}}$ eliminates the time derivative of the angular velocity along the spin axis. Likewise, the axial symmetry of the rotor ensures that the cross product of $\boldsymbol{\omega}^{\times}\mathbf{I}_r(\boldsymbol{\omega} + \mathbf{a}\omega_s)$ does not contribute to the torque about the rotor's spin axis. Equations (4.11)– (4.13) can also be used together with the analytical solution presented in Section 3.2. Replacing the time derivatives of the angular velocities with their respective expressions from equations (3.14) and (3.15) we find:

$$g_{r2} = \omega_3\omega_1\left[\frac{I_t(I_3 - I_1)}{I_2} + (I_s - I_t)\right] + \omega_3\omega_s\left[I_s - \frac{I_sI_t}{I_2}\right] \tag{4.14}$$

$$g_{r3} = \omega_2\omega_1\left[\frac{I_t(I_1 - I_2)}{I_3} + (I_t - I_s)\right] + \omega_2\omega_s\left[\frac{I_sI_t}{I_3} - I_s\right] \tag{4.15}$$

In general, these transverse torques are responsible for the reaction forces that the magnetic bearing needs to produce to keep the rotor suspended and centered. A common assumption for stationary magnetic bearings, is to analyze each axis separately. We apply this assumption here as well, since g_{r2} and g_{r3} are decoupled. All of the information needed to calculate the transverse torques is readily available in spacecraft. Rate sensors provide the angular velocities of the spacecraft and the controls on the motors of the momentum wheels keep track of the relative wheel speeds. The angular accelerations can usually be calculated by a finite difference method or a more sophisticated filtering technique. It is therefore possible to calculate the transverse torques during a maneuver.

The transverse torques acting on the rotor will cause it to rotate about its center of mass. We can simply state that each torque is caused by a force F on the rotor at a distance $L/2$ from the rotor's center of mass, where L is the distance from the center of mass (CM) to the centerline of the radial magnetic bearings. Here we assume that the bearings are located equidistant from the CM. Depending on the configuration of the system, the rotor can be supported by one or two bearings. Based on the MBRotor kit that we use as a benchmark throughout this analysis, the shaft is suspended in two magnetic bearings. A detailed description of the MBRotor kit is included in Appendix B. The two bearings therefore share the load caused by the transverse torques. Continuing with the case of a rotor aligned with the $\hat{b}_1$ axis, we can write the scalar equations of the forces in the magnetic bearings as:

$$F_2 = \frac{g_{r2}}{L} = \frac{1}{L}\big(I_t\dot{\omega}_2 + \omega_1\omega_3(I_s - I_t) + I_s\omega_s\omega_3\big) \tag{4.16}$$

$$F_3 = \frac{g_{r3}}{L} = \frac{1}{L}\big(I_t\dot{\omega}_3 + \omega_1\omega_2(I_t - I_s) - I_s\omega_s\omega_2\big) \tag{4.17}$$

The expression (4.16) and (4.17) represent the forces acting on the rotor expressed in the rotating reference frame $\mathcal{F}_B$ and only describe the forces due to the interaction of the rotor and the platform. As such, certain forces, such as imbalance forces, are not included in equations (4.16) and (4.17). At higher rotational speeds, slight bows in the rotor shaft or

other imbalances in the disks will cause eccentricities in the shaft's orbit. The result will be cyclical forces that must be compensated by the magnetic bearings. These imbalance forces can be reduced by balancing the rotor system and by tuning the stiffness and damping values of the magnetic fields. In this respect, magnetic bearings provide an advantage over anti-friction bearings, since the stiffness and damping effects of the magnetic field can be modified.

The torques, as expressed in equations (4.12) and (4.13), are functions of ten parameters, several of them embedded in the equations of $\dot{\omega}_2$ and $\dot{\omega}_3$. In this list, we exclude the three principal moments of inertia of the entire platform–rotor system, which we assume to remain constant. The remaining relationships can be expressed as:

$$g_{r2} = g\big(\omega_1, \omega_2, \omega_3, \omega_s, I_s, I_t, g_a, g_{ex1}, g_{ex2}, g_{ex3}\big) \tag{4.18}$$

$$g_{r3} = g\big(\omega_1, \omega_2, \omega_3, \omega_s, I_s, I_t, g_a, g_{ex1}, g_{ex2}, g_{ex3}\big) \tag{4.19}$$

We study the nature of each individual dependency by varying each parameter individually, while holding the others constant. To begin, we pick a meaningful nominal set of values that describe the Whorl–1 model. We choose the angular velocities of $\mathcal{F}_\mathcal{B}$ to be $(0.5, 0.5, 0.8)$ rad/s. This choice corresponds to the estimated maximum angular velocities of Whorl–1 when only the reaction wheels are used as actuators. As a reference value of the relative angular velocity ω_s we pick 7000 RPM or approximately 730 rad/s. This value is roughly in the mid–range of the possible rotor speeds. The MBRotor kit has a maximum possible speed of 15,000 RPM. Through preliminary testing we find that the first critical speed of the magnetic bearing rotor system is between 3200–3300 RPM and the second critical is in the range of 8300–8400 RPM. The reference value of 7000 RPM is therefore sufficiently below the second critical, such that the imbalance effects are still relatively small. Similarly to Whorl–1, the rotor's inertia parameters are based on a CAD model analysis. The principal moments of inertia are:

$$\mathbf{I}_R = \begin{bmatrix} 0.00039 & 0 & 0 \\ 0 & 0.11 & 0 \\ 0 & 0 & 0.11 \end{bmatrix} \quad [\text{kg m}^2] \tag{4.20}$$

The four torque parameters are treated slightly differently. Since the axial torques are time–variant and dependent on a specific control law, we set the nominal $g_a = 0$. The three external torques are also nominally set to zero.

With these reference conditions, which are also used in the following sections, we can take a closer look at the dependencies expressed by equations (4.18) and (4.19). Here, we study

each parameter individually without introducing the dynamic interdependencies. At first glance we note that both g_{r2} and g_{r3} vary linearly with all ten parameters. However, we find that neither the axial torque g_a nor the external torque g_{ex1} have any effect. Both these torques act about the $\hat{b}_1$ axis and therefore have no influence on either g_{r2} or g_{r3}. The decoupling of the torques about the $\hat{b}_1$ axis is determined by the rotor's spin axis. If the rotor's spin axis is not aligned with $\hat{b}_1$ this decoupling does not occur. Furthermore, we see that the external torques on the gyrostat directly affect the rotor as well. Each transverse torque increases linearly with its corresponding external torque.

The responses to the variations in the angular velocities of $\mathcal{F}_\mathcal{B}$ highlights the converse effects of ω_1 and ω_s. Increases in either of these rates will increase g_{r3} and decrease g_{r2}. Ultimately, both torques become zero, leading to the conclusion that by spinning the gyrostat and the rotor about the same axis, the transverse torques can be minimized. This scenario corresponds to case B and case C, two of the possible equilibrium cases described by Hughes.[2] In both cases, the gyrostat and rotor are spinning about the same axis. Equations (4.12) and (4.13) indicate that both torques become zero for any spin purely about the $\hat{b}_1$ axis. This conclusion is also supported by the results of plotting the two transverse torques as functions of ω_2 and ω_3. As can be further seen from equations (4.12) and (4.13), each transverse torque is dependent on its perpendicular angular velocity, *i.e.* $g_{r2} = g(\omega_3)$ and $g_{r3} = g(\omega_2)$. These relationships become important in later analysis.

Varying the inertias of the rotor shows that the shape of the rotor affects the transverse torques as well. Figure 4.1 indicates that we can minimize the transverse torques by increasing the transverse inertia and reducing the axial inertia. We conclude that a more cylindrical shaped rotor experiences smaller transverse torques than a thin disk. The theoretical limits of this behavior can be found by taking limits of equations (4.14) and (4.15). The torques are minimized by letting the axial inertia I_s tend towards zero.

$$\lim_{I_s \to 0} g_{r2} = \omega_1 \omega_3 I_t (A - 1) \qquad \text{where} \quad A = \frac{I_3 - I_1}{I_2} \tag{4.21}$$

$$\lim_{I_s \to 0} g_{r3} = \omega_1 \omega_2 I_t (B + 1) \qquad \text{where} \quad B = \frac{I_1 - I_2}{I_3} \tag{4.22}$$

The minimum torques for the nominal conditions are included in equations (4.21) and (4.22). We observe that both the minimum and the maximum torques are dependent on the inertia parameters of the gyrostat. To obtain expressions from the maximum torques, we set the axial inertia equal to a multiple of the transverse inertia, $I_s = mI_t$. The parameter m defines the ratio between the two inertias. Using equations (**??**) and (4.15) we express the maximum

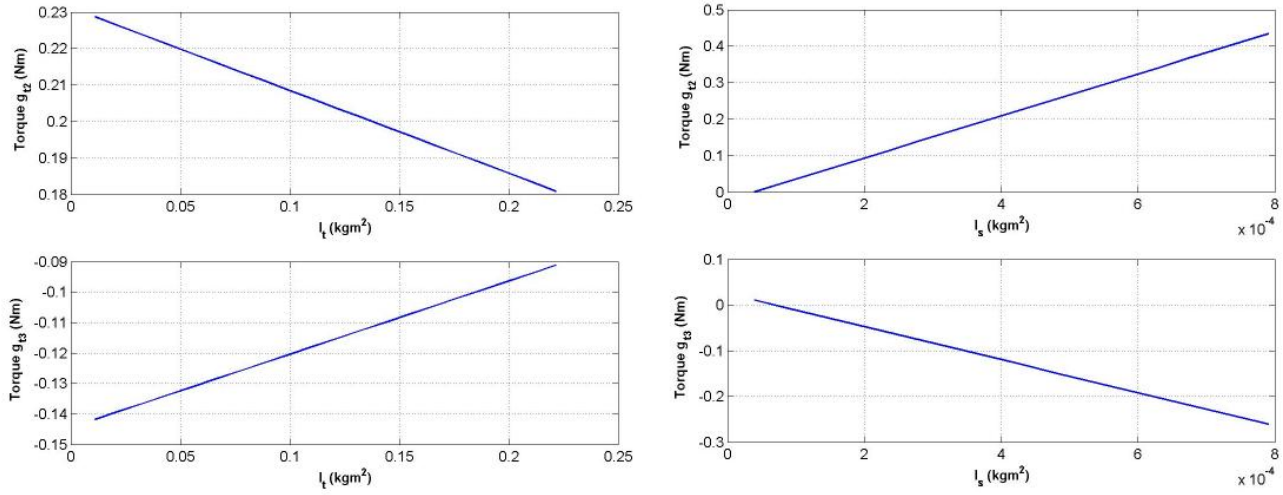

Figure 4.1: *Transverse Torques g_{r2} and g_{r3} as Functions of the Transverse and Axial Rotor Inertias*

torques in terms of the parameter m as:

$$g_{r2max} = \omega_1\omega_3 I_t\big(A + m - 1\big) + \omega_3\omega_s m I_t \left(1 - \frac{I_t}{I_2}\right) \tag{4.23}$$

$$g_{r3max} = \omega_1\omega_2 I_t\big(B + 1 - m\big) + \omega_2\omega_s m I_t \left(\frac{I_t}{I_3} - 1\right) \tag{4.24}$$

If the rotor is to be used as a momentum actuator, a decrease in the axial inertia is usually not desirable, since it limits the maximum value of angular momentum of the actuator. These trade–offs can now be taken into consideration when designing a rotor where the transverse torques become an important factor.

Having determined the dependencies of the eight parameters that appear in the transverse torque equations, we are now interested in the effects of these variables over time. We therefore consider four major scenarios that lead to the numerical simulations described in Section 3.3. We begin with a torque–free gyrostat. The following two scenarios discuss controlled attitude maneuvers. The fourth scenario focuses on a gyrostat with constant external torques.

4.2 Gyrostat with No External or Axial Torques

The first case we investigate is a gyrostat with no external torques. The gyrostat is either tumbling or spinning about its major axis with constant angular momentum. The rotor itself is also decoupled from its drive motor and there are no torques due to motor action or due to frictional losses. As the overall angular momentum of the gyrostat remains constant, the magnitudes of the angular velocities of the platform remain bounded. For this case, we return to equations (4.14) and (4.15). We continue to assume that the rotor's spin axis is aligned with the $\hat{b}_1$ axis.

Altogether, there are five parameters that can be varied in equations (4.14) and (4.15). These parameters are the moments of inertia of the rotor as well as the initial conditions of the body and relative angular velocities. Since we are numerically integrating the gyrostat's equations of motion over time, all five parameters are only varied independently prior to the numerical integration. The remaining parameters are set to the nominal values described above. Most graphs resulting from these simulations show the resulting forces as opposed to the torques. These two quantities are proportional to each other. The responses over time, therefore, are only scaled by the distance from the center of mass to the point at which the forces are acting. Graphing the forces, rather than the torques, facilitates the discussion in Chapter 5 as we examine the effects these forces have on the magnetic bearings.

Figure 4.2 shows both F_2 and F_3 at the nominal values as defined in the previous section. The oscillatory behavior parallels that of the angular velocities. In fact, we can see from Figure 4.2 that the forces share the same period with their perpendicular angular velocity, and that F_3 and ω_2 are 90° out of phase. We encounter this correspondence in the period, and therefore in the frequency, throughout the gyrostat simulations.

Since the initial conditions for the angular velocities for the simulations recorded in Figures 4.2 are the estimated values, we note that the magnitude of both forces are small. We therefore examine the influence of the initial condition angular velocities on forces by varying each of them individually while holding all other parameters constant.

Figure 4.3 shows a plot of the frequencies of the forces F_2 and F_3 versus the initial angular velocities. We observe that both forces have the same frequency behavior as we vary the angular velocities. Since ω_s is several magnitudes larger the body angular velocities, we adjust its scale to compare all four sets of data on the same graph. We note that the

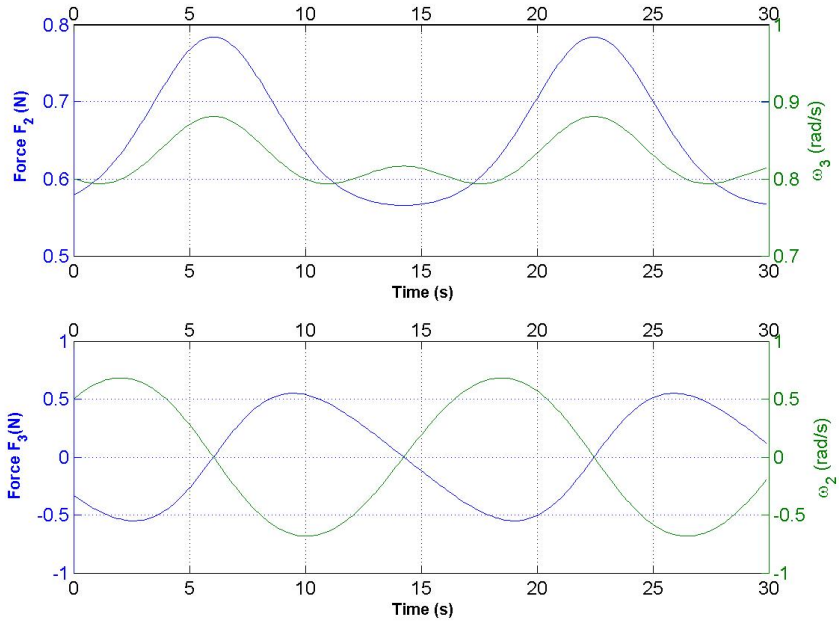

Figure 4.2: *Forces F_2 and F_3 Acting on the Rotor of a Torque-Free Gyrostat*

frequencies for both forces vary little with changes in ω_1, ω_2 and ω_s. Only ω_3 shows a linear relationship with the frequency of both forces. Varying these initial conditions affects both the frequency and the magnitudes of the forces. As the gyrostat is spinning faster, we expect both parameters to increase.

Whereas the frequency dependency of both forces is the same, the amplitudes behave differently. From previous observations, namely equations (4.14) and (4.15), we expect F_2 to be a function of ω_3 and F_3 to vary with ω_2. Figures 4.4 and 4.6 illustrate the relationship between the amplitude of the forces and the angular velocities. In both cases, increases in ω_1 and ω_2 result in an almost identical behavior. While all four angular velocities affect the amplitude of F_2, we note that both for ω_3 and ω_s the rate of change of the amplitude is smaller. We also observe that $F_2(\omega_3)$ reaches a minimum at a value of $\omega_3 \approx 0.5$, *i.e.* when all three body angular velocities are equal.

Referring to Figure 4.2, we note that F_2 oscillates about a nonzero mean value. As we increase the angular velocity ω_3, this mean value also increases. Thus even while the amplitude changes at a smaller rate, the overall effect leads to a larger transverse force F_2. We illustrate

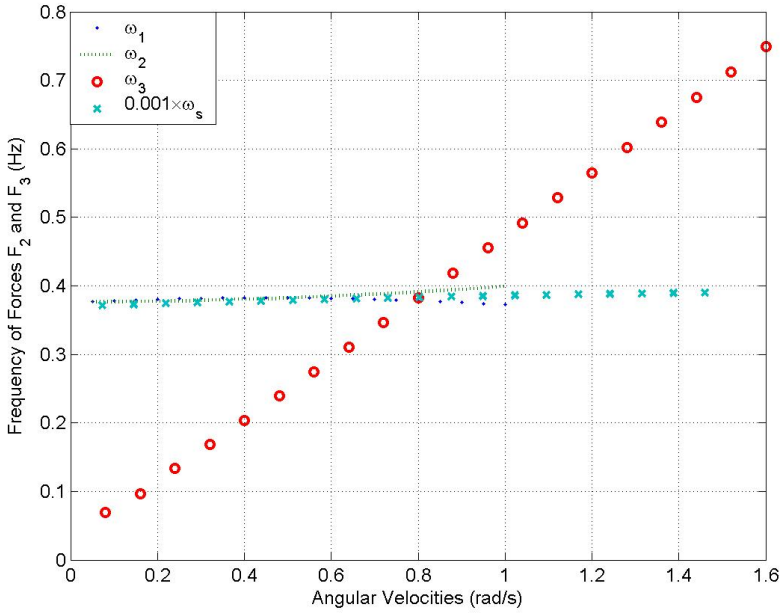

Figure 4.3: *Frequency vs Initial Angular Velocity Plot for F_2 and F_3 of the Torque–Free Gyrostat*

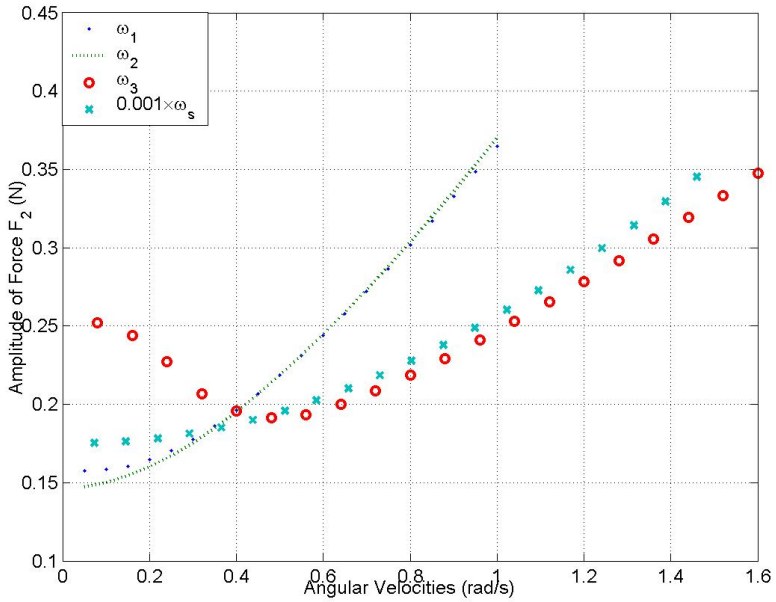

Figure 4.4: *Amplitude of Force F_2 vs Initial Angular Velocity for the Torque–Free Gyrostat*

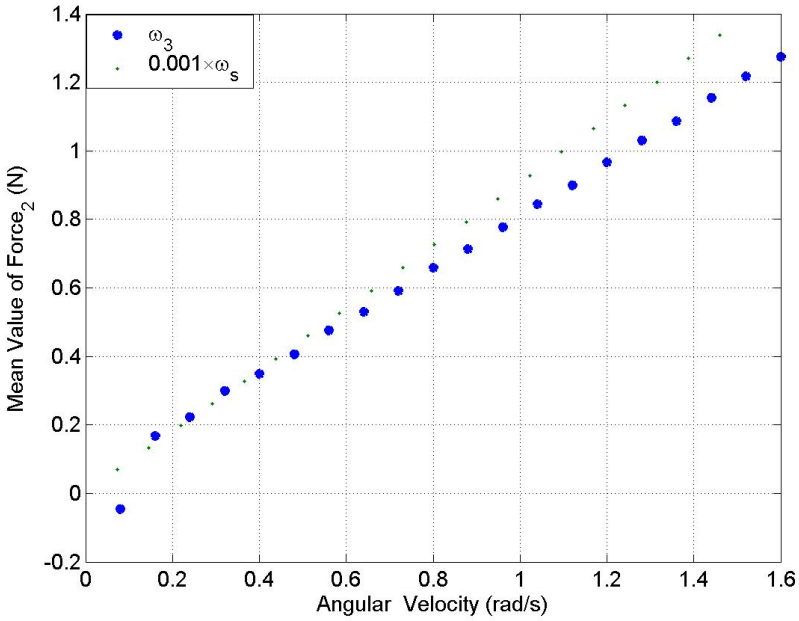

Figure 4.5: *Mean Values of the Force F_2 as a Function of ω_3 and ω_s for the Torque–Free Gyrostat*

the relationship between the mean value of the force F_2 and the angular velocities ω_3 and ω_s in Figure 4.5.

Figure 4.6 shows the amplitudes of the force F_3 for varying angular velocity parameters. We observe that the amplitude of F_3 remains constant as ω_3 changes. The largest rate of change in the amplitude of F_3 is associated with ω_1 and ω_2. Both angular velocities result in identical parabolic curves. Comparing these curves with Figure 4.4, we see that ω_1 and ω_2 result in similar behavior for both forces. The relative spin rate ω_s causes the amplitude to increase linearly, which is in contrast to the effects of ω_s on the force F_2. Unlike F_2, the mean value of force F_3 remains zero throughout these variations. We conclude that increasing ω_s results in larger mean values for F_2 and increases the amplitude of F_3.

Overall, we find that increases in the initial values of ω_1, ω_2 and ω_s all effectively lead to larger amplitudes for both F_2 and F_3. On the other hand, ω_3 influences the frequency of the oscillations. While we see only an increase in the frequency of F_3, the force F_2 also increases in the mean value of its magnitude. Here, we observe the previously mentioned dependencies of $g_{r2} = g(\omega_3)$ and $g_{r3} = g(\omega_2)$.

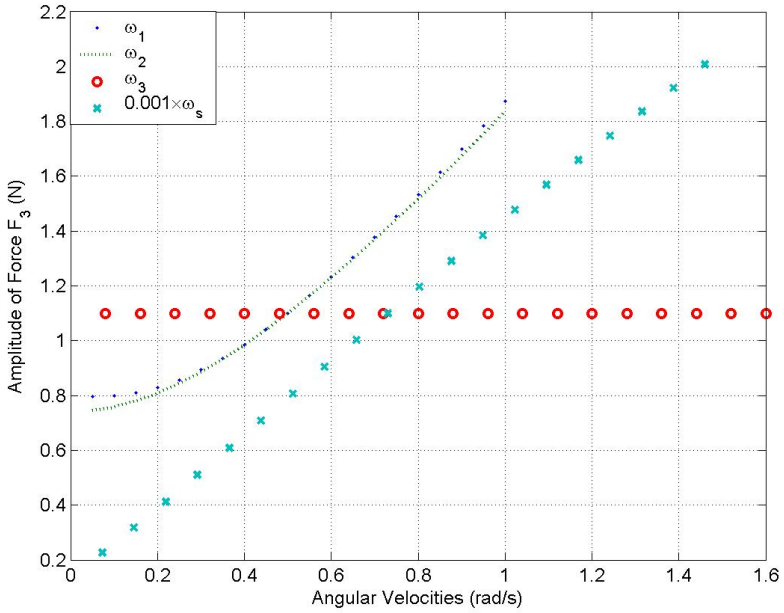

Figure 4.6: *Amplitude of Force F_3 vs Initial Angular Velocities for the Torque–Free Gyrostat*

Having considered several variations in the initial angular velocities, we explore the effects of changing the rotor geometry. To evaluate the forces on the shaft for a varying rotor geometry, we model the rotor as a shaft and a single disk. We then vary both the transverse and axial inertias individually. Since we are still exploring the torque–free gyrostat, the results of these variations remain sinusoidal. Figures 4.7 and 4.8 highlight the influence of the inertias on the frequency and amplitude of the forces F_2 and F_3. We observe that the transverse inertia I_t has no impact on the frequency. The frequencies of both forces remain constant. The axial inertia, on the other hand, does affect the frequency. The values of the inertias I_t and I_s range from 0.1 to twice the nominal values described before. We note that the magnitude of I_s is smaller than that of I_t. The plotted values for I_s in both graphs therefore over a shorter span, even though they represent the same number of sample points.

The effects of I_t and I_s on the amplitudes of the forces F_2 and F_3 are not as pronounced as their effects on the frequencies. While the impact is still relatively small, increasing the transverse inertia affects the amplitudes of both forces. We also see that strongest relationship exists between the axial inertia I_s and the force F_3.

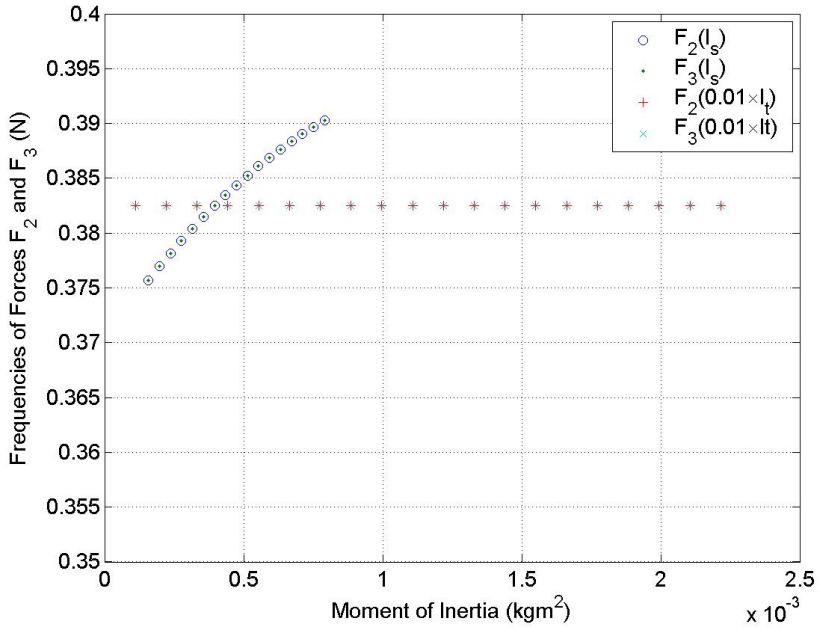

Figure 4.7: *Frequency Response of Forces F_2 and F_3 as Functions of the Inertias I_t and I_s*

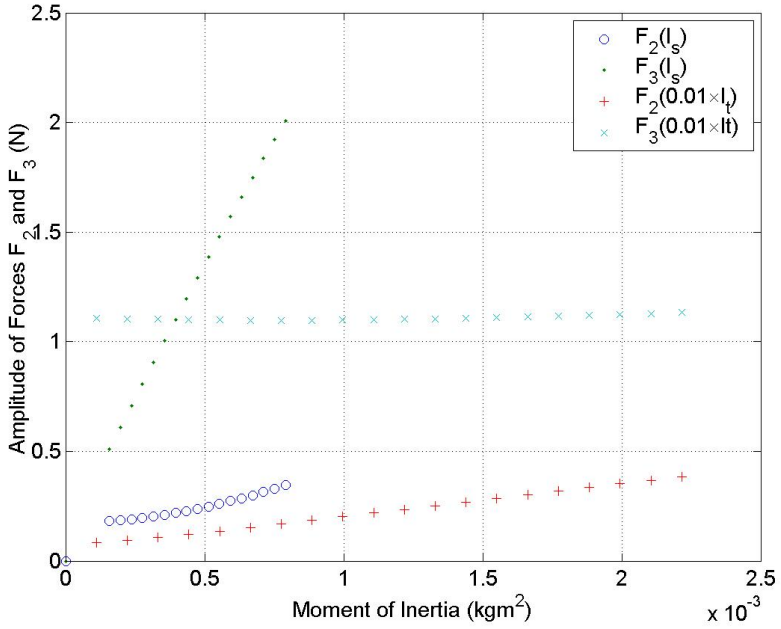

Figure 4.8: *Amplitudes of Forces F_2 and F_3 as Functions of the Inertias I_t and I_s*

Throughout the variations in the angular velocities and the inertias, we notice that certain parameters influence the frequency of the forces F_2 and F_3, while others do not. The frequency of the forces corresponds to the natural frequency of the gyrostat's motion. To determine this natural frequency, we linearize the equations of motion about a desired equilibrium. We return to the equations of motion presented in section 3.2, and reprint them here for convenience:

$$\dot{\omega}_1 = \frac{I_2 - I_3}{I_P}\omega_2\omega_3 \tag{4.25}$$

$$\dot{\omega}_2 = \frac{I_3 - I_1}{I_2}\omega_3\omega_1 - \frac{I_s}{I_2}\omega_3\omega_s \tag{4.26}$$

$$\dot{\omega}_3 = \frac{I_1 - I_2}{I_3}\omega_1\omega_2 + \frac{I_s}{I_3}\omega_2\omega_s \tag{4.27}$$

We would like to find an equilibrium that will describe a motion mainly about the $\hat{b}_3$ axis. If we therefore prescribe that $\omega_3 = \Omega$, we find an overall solution for an equilibrium motion based on equations (4.25) and (4.27). This equilibrium becomes:

$$\boldsymbol{\omega}_e = \begin{bmatrix} \frac{h_s}{I_3 - I_P} \\ 0 \\ \Omega \end{bmatrix} \tag{4.28}$$

Assuming small perturbations of $\delta\omega_i$, about the equilibrium $\boldsymbol{\omega}_e$, we find that:

$$\boldsymbol{\delta\omega} = \begin{bmatrix} \delta\omega_1 + \frac{h_s}{I_3 - I_P} \\ \delta\omega_2 \\ \delta\omega_3 + \Omega \end{bmatrix} \tag{4.29}$$

Taking the time derivative of equation (4.29), we can write the linearized equations of motion as:

$$\boldsymbol{\delta\dot{\omega}} = \begin{bmatrix} 0 & \frac{I_2 - I_3}{I_1 - I_s}\Omega & 0 \\ \frac{I_3 - I_1 + I_s}{I_2}\Omega & 0 & 0 \\ 0 & \frac{(I_3 - I_2)h_s}{I_3(I_3 - I_1 + I_s)} & 0 \end{bmatrix} \begin{bmatrix} \delta\omega_1 \\ \delta\omega_2 \\ \delta\omega_3 \end{bmatrix} \tag{4.30}$$

Solving for the eigenvalues of the 3×3 matrix of equation (4.30) we find:

$$\lambda_1 = 0 \tag{4.31}$$

$$\lambda_{2,3} = \pm j\Omega\sqrt{\frac{(I_3 - I_2)(I_3 - I_1 + I_s)}{I_2(I_1 - I_s)}} \tag{4.32}$$

From linear system theory, we know that the imaginary components of the eigenvalues of the state transition matrix are the natural frequency of the system. Substituting in for the inertia parameters given in (3.8) we find:

$$\lambda_{2,3} = \pm 0.46552 j\Omega \tag{4.33}$$

The natural frequency of the system therefore becomes:

$$\omega_n = I_n \Omega \qquad \text{where} \qquad I_n = \sqrt{\frac{(I_3 - I_2)(I_3 - I_1 + I_s)}{I_2(I_1 - I_s)}} \tag{4.34}$$

From equation (4.34) we clearly see that besides the three inertia parameters of the overall gyrostat, only the angular velocity about the $\hat{b}_3$ axis and the axial rotor inertia affect the frequency of oscillation. This relationship corresponds directly with the results from the parameter studies. We observe this correspondence in Figure 4.2.

The last variation we explore for the torque–free gyrostat is the direction of the spin axis of the rotor. This option is currently not available with the actual Whorl–1 simulator. The spin axis of the magnetic bearing system is fixed on the simulator's top deck. However, we can relax this constraint in the numerical model.

We introduce an angle θ such that the components of the spin axis $\mathbf{a}$ are functions of this angle. We can therefore evaluate the effect of varying the spin axis in a specific plane. For instance, if we are interested in the $\hat{b}_1\hat{b}_2$–plane, we define

$$\mathbf{a} = \begin{bmatrix} \cos\theta \\ \sin\theta \\ 0 \end{bmatrix} \tag{4.35}$$

Since the inertia matrix of the rotor is written in the $\mathcal{F}_\mathcal{B}$ reference frame, we also need to define a new nodal reference frame $\mathcal{F}_\mathcal{R}$. This frame is defined such that the rotor spin vector $\mathbf{a}$ is aligned with the $\hat{r}_1 = (1, 0, 0)$ axis. As we vary the direction of the spin axis $\mathbf{a}$, the rotor frame $\mathcal{F}_\mathcal{R}$ rotates with respect to the body frame $\mathcal{F}_\mathcal{B}$. To continue using equation (4.6), the moments of inertia of the rotor need to be known in $\mathcal{F}_\mathcal{B}$. Therefore, we rotate the new moment of inertia matrix back into the body–fixed reference frame.

As the spin axis $\mathbf{a}$ sweeps the $\hat{b}_1$–$\hat{b}_2$ plane, we see in Figure 4.9 that the maximum value of force F_2 is minimized when the rotor is parallel to the $\hat{b}_1$ axis. The spin axis is defined as in equation (4.35). An angle of $\theta = 0°$ aligns the spin axis of the rotor with the $\hat{b}_2$ vector. We

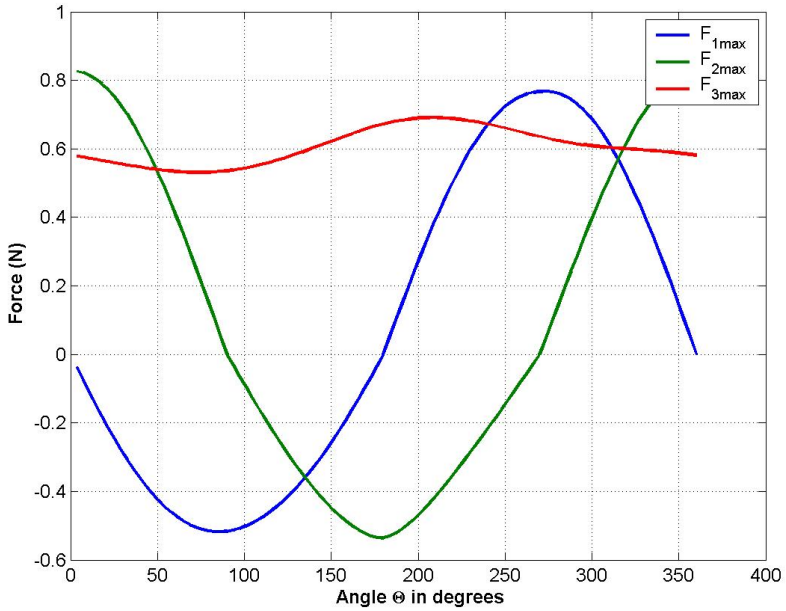

Figure 4.9: *Maximum Values of Forces F_1,F_2 and F_3 for a Varying Spin Axis in the XY–Plane*

observe the trade–off between F_1 and F_2 as we sweep the spin axis from one principal axis to another. At the intermediate angle, we observe the influence of the change in axial angular momentum on the force F_3. Even though we are not applying any axial torques, there is a limited exchange of angular momentum between the rotor and the platform.

The transverse torques are influenced by both the motion of the platform and the shape and relative spin of the rotor. We observe that the frequency of the torques is equivalent to the natural frequency of the gyrostat's motion. For a given equilibrium, we can determine this frequency by analyzing the linearized equations of motion. The magnitudes of the internal forces are low, with an upper limit of 2 N throughout the range of the possible motions. The next section explores the effects of two types of maneuvers on the transverse torques.

4.3 Momentum Wheel Attitude Maneuvers

Momentum or reaction wheels are routinely used in satellites as attitude actuators. While the previous discussion is interesting from a dynamics point of view, most momentum wheels

supported by magnetic bearings will experience axial torques. Likewise, magnetically suspended flywheels will more often be subjected to controlled attitude changes than uncontrolled tumbling. As such we can study two scenarios in which the gyrostat undergoes simple maneuvers. In the first case, the gyrostat undergoes an attitude slew in order to reorient itself. Continuing with the Whorl–1 model as a basis for these simulations, we choose a simple 90° slew about the $\hat{b}_3$ axis. The second maneuver we evaluate is a steady spin about the $\hat{b}_3$ axis. For both cases there are no external torques on the gyrostat. We note that the rotor of the magnetic bearing system is not used as an actuator in either of these maneuvers. The control torques determined by the control law are applied only to the three momentum wheels on Whorl–1.

We implement a simple state feedback linearization control law derived from equation (4.10). The control law is derived using Lyapunov's direct method.[22] We begin with the following Lyapunov Function:

$$V = \frac{1}{2}\boldsymbol{\omega}^T \mathbf{J}\boldsymbol{\omega} + \boldsymbol{\sigma}^T \mathbf{K}_\sigma \boldsymbol{\sigma} \tag{4.36}$$

Here, $\boldsymbol{\sigma}$ refers to the Modified Rodriguez Parameters (MRP). The kinematic equations associated with the MRPs are given by:

$$\dot{\boldsymbol{\sigma}} = G(\boldsymbol{\sigma})\boldsymbol{\omega} \tag{4.37}$$

where

$$G(\boldsymbol{\sigma}) = \frac{1}{2}\left(\mathbf{1} + \boldsymbol{\sigma}^\times + \boldsymbol{\sigma}\boldsymbol{\sigma}^T - \frac{1+\boldsymbol{\sigma}^T\boldsymbol{\sigma}}{2}\mathbf{1}\right) \tag{4.38}$$

We assume here that the three momentum wheel actuators are all aligned with the principal axes, such that $\mathbf{A}$ becomes the identity matrix. The rotor (the fourth wheel) is not actuated. As stated before, we are excluding the effects of external torques such that $\mathbf{g}_{ex} = \mathbf{0}$. The control law resulting from this Lyapunov function is:

$$\mathbf{A}\mathbf{g}_a = \mathbf{g}_e + \boldsymbol{\omega}^\times \mathbf{h} + \mathbf{K}_\omega \delta\boldsymbol{\omega} - G(\sigma)\mathbf{K}_\sigma \delta\boldsymbol{\sigma}^T \tag{4.39}$$

Both $\mathbf{K}_\omega$ and $\mathbf{K}_\sigma$ are 3×3 diagonal gain matrices that multiply the angular velocities of $\mathcal{F}_B$ and the vector of the Modified Rodriguez Parameters (MRP) respectively. If we solve for $\dot{V}$ and substitute in equation (4.39) we find that:

$$\dot{V} = -\boldsymbol{\omega}^T K_\omega \boldsymbol{\omega} \tag{4.40}$$

The time derivative $\dot{V}$ is therefore negative semi–definite and stabilizes the system at the origin. To prove asymptotic stability we invoke LaSalle's Theorem.[22] From equation (4.40)

we see that the angular velocities are bounded. The difference between the reference and the current angular velocities is given by:

$$\delta\boldsymbol{\omega}(t) = \boldsymbol{\omega}_r - \boldsymbol{\omega}(t) \tag{4.41}$$

We note that

$$\lim_{t\to\infty} \delta\boldsymbol{\omega} = \mathbf{0} \tag{4.42}$$

Substituting the control law (4.39) into equation (4.10) we find:

$$\mathbf{J}\dot{\boldsymbol{\omega}} = \mathbf{K}_\omega \delta\boldsymbol{\omega} - G(\boldsymbol{\sigma})\mathbf{K}_\sigma \delta\boldsymbol{\sigma}^T \tag{4.43}$$

Since $\lim_{t\to\infty} \boldsymbol{\omega} = \mathbf{0}$ its time derivative $\dot{\boldsymbol{\omega}}$ also tends towards zero [23]. Equation (4.43) only holds if:

$$\lim_{t\to\infty} \delta\boldsymbol{\omega} = \mathbf{0} \tag{4.44}$$

LaSalle's Theorem is therefore satisfied and the control law (4.39) globally asymptotically stabilizes the equilibrium attitude. The control law to achieve a steady spin is derived similar to equation (4.39), but without the attitude reference. We find:

$$\mathbf{A}\mathbf{g}_a = \mathbf{g}_e + \boldsymbol{\omega}^\times \mathbf{h} + \mathbf{K}_\omega \delta\boldsymbol{\omega} \tag{4.45}$$

Once again, LaSalle's Theorem shows this control law globally asymptotically stabilizes the desired steady spin equilibrium.

As mentioned before, we begin by exploring a 90° slew maneuver. The initial values are set to the nominal condition described in Section 4.1. Figure 4.10 shows the response of both transverse torques at the nominal values. The gains of the controller in equation (4.39) are not selected to provide a minimal time for the maneuver. Instead, their values are chosen to highlight the relationship between the angular velocities and the transverse torques. After an initial transient period, we observe again the correspondence in frequency between the angular velocities and the transverse torques. As Whorl–1 approaches its desired attitude, both transverse torques become zero.

We also note that the peak torques occur at the beginning of the maneuver. Overall, even these peak values remain small. Figures 4.11 and 4.12 show the overshoot of the transverse torques as functions of the initial velocities. The initial angular velocities are variations of the nominal values. As with the torque–free gyrostat, we investigate a range of up to twice the nominal values. The upper limit of this range is given by $(1, 1, 1, 6)$ rad/s for the body

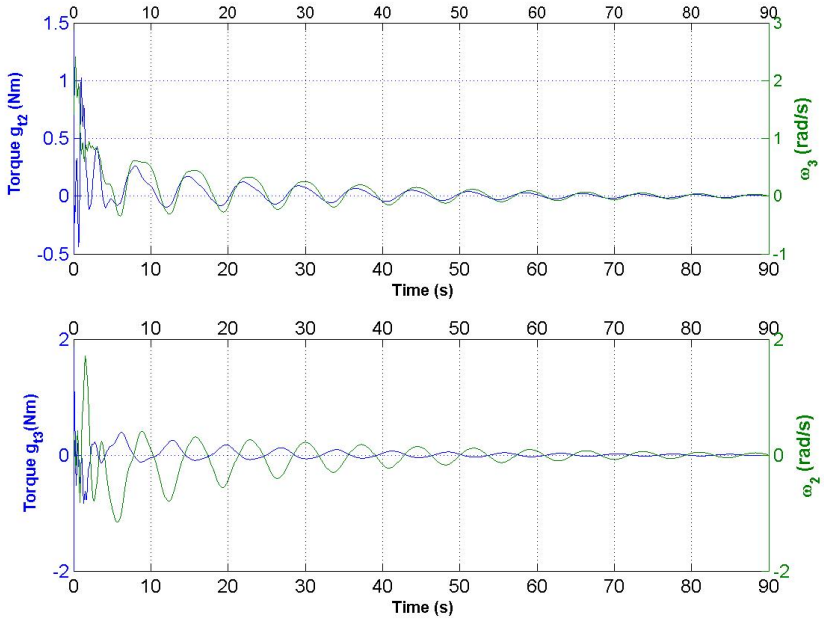

Figure 4.10: *Transverse Torque g_{r2} and g_{r3} Plotted with ω_3 and ω_2 Respectively*

angular velocities, and 1500 rad/s for the relative spin ω_s. As we increase the initial body angular velocities, the control effort rises. The maneuver becomes more abrupt. However, we see in Figure 4.11 that only the relative spin ω_s increases F_2. A similar result is illustrated in Figure 4.12. The largest overshoot in F_3 is caused by ω_s. The graphs in these figures do not represent continuous functions. The discontinuities we observe are the result of a low sampling rate.

The overall magnitudes of both forces are large compared to the torque–free case. The largest forces of approximately 3.55 N are achieved at the maximum spin of the rotor at 15,000 rpm.

On the other hand, when we desire a steady spin we find that the transverse torques reach constant values. Based on the Whorl–1 model, we prescribe a steady spin about the $\hat{b}_3$ axis. For a spin of $\boldsymbol{\omega} = (0, 0, \Omega)$, we expect F_3 to go to zero and F_2 to approach a constant value. Figure 4.13 shows the familiar plot of the transverse torques and their perpendicular angular velocities. The steady–spin maneuver begins with the nominal conditions and achieves a spin of $\boldsymbol{\omega} = (0, 0, 1)$. As with the previous attitude controller, both torques experience a

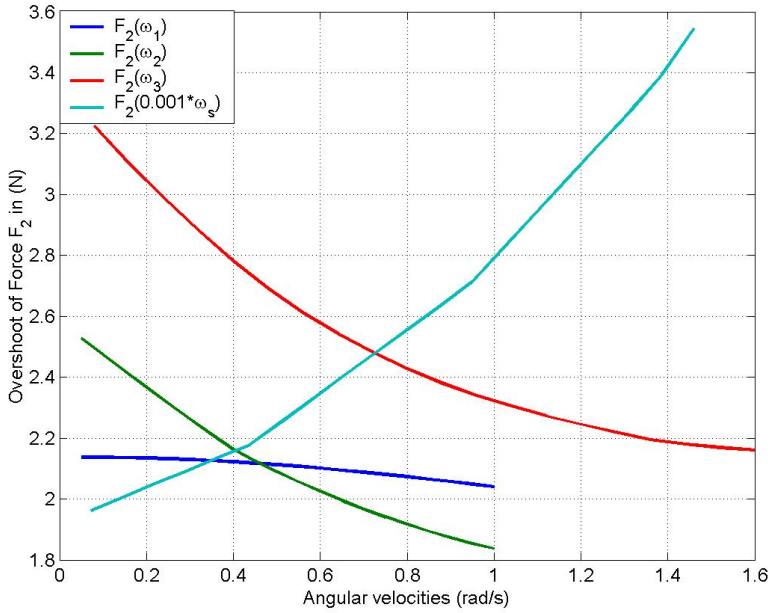

Figure 4.11: *Overshoot of Force F_2 as a Function of the Angular Velocities*

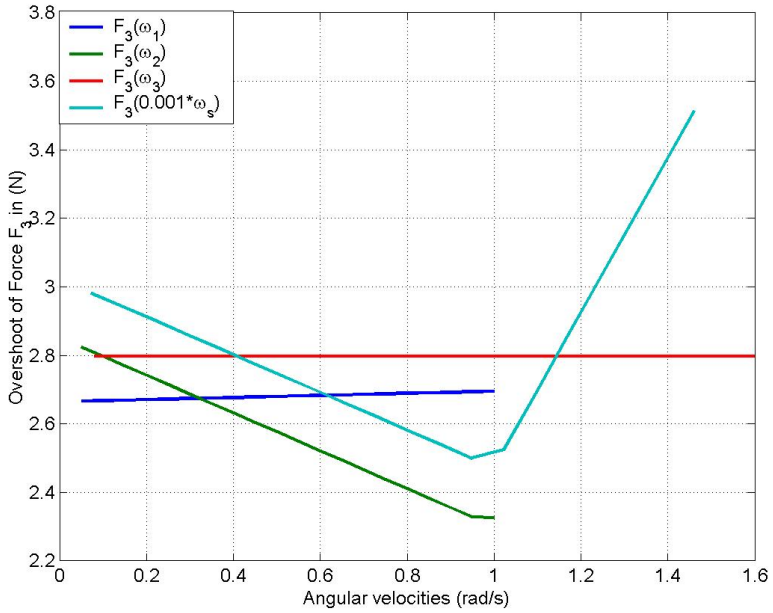

Figure 4.12: *Overshoot of Force F_3 as a Function of the Angular Velocities*

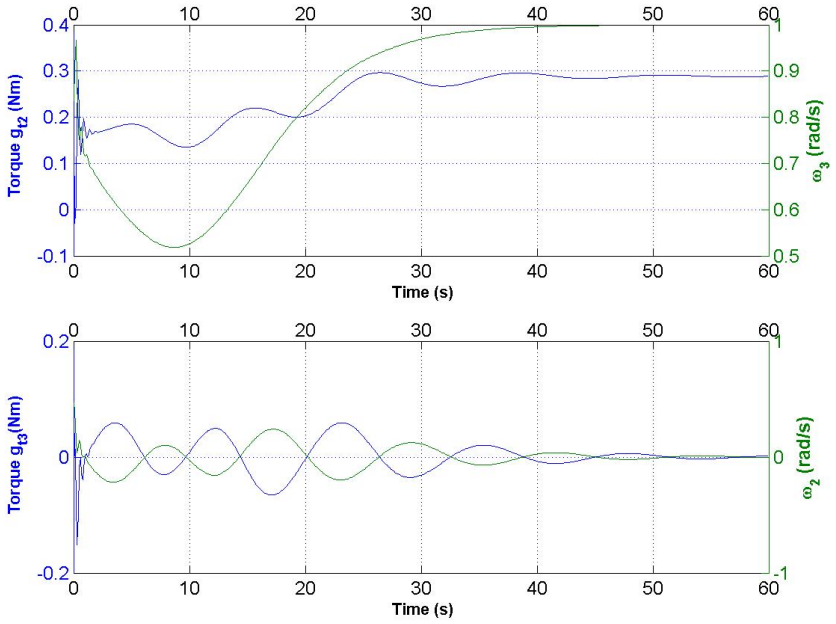

Figure 4.13: *Transverse Torques g_{r2} and g_{r3} Plotted with Angular Velocities ω_3 and ω_2 Respectively*

short transient period, which leads into an decaying oscillatory behavior.

The influence of the angular velocities on the maximum force for this maneuver are depicted in Figures 4.14 and 4.15. For the same range of angular velocities, we observe smaller overall forces for this maneuver than for the 90° slew maneuver. The rotor spin ω_s has the largest effect on both forces. Furthermore, the final values of the force F_2 increase linearly with ω_s.

The overall magnitudes of both forces are in a similar range as the forces of the torque–free case. We observe a maximum of approximately 1.5 N for F_2 at maximum rotor speed. The settling time of either force is not affected by the variations in the angular velocities.

Both attitude maneuvers show the same correspondence in frequency between the forces and their perpendicular angular velocities. We notice that the maximum forces remain below 3.6 N. The relative spin of the rotor has the largest effect on the magnitudes of both forces. The final case we explore is a gyrostat with external torques. Here, we apply a timed external torque without feedback controller.

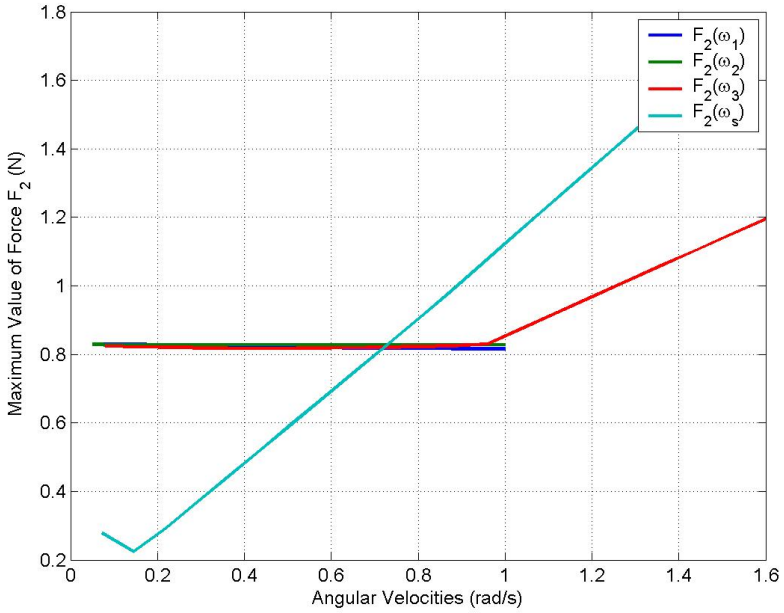

Figure 4.14: *Maximum Values of the Force F_2 as a Function of the Angular Velocities ω_3 and ω_2*

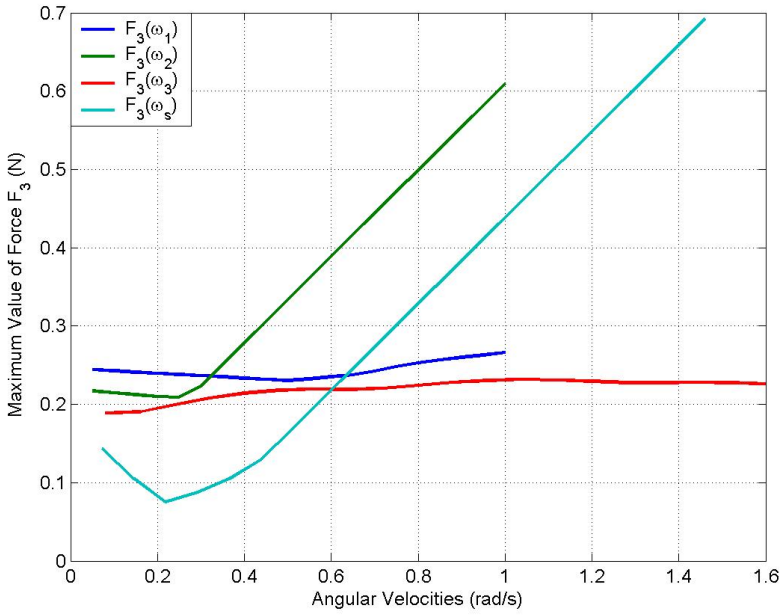

Figure 4.15: *Maximum Values of the Force F_3 as a Function of the Angular Velocities ω_3 and ω_2*

4.4 Momentum Wheel Attitude Maneuvers with External Torques

In this section, we focus on the effects of external torques on the rotor–platform interactions. Whorl–1 is equipped with several small gas thrusters, mounted together on the outer edge of the bottom platform. The mounting bracket and the gas regulator can be seen in the bottom left corner in Figure A.1. Each thruster can produce slightly under 1 N of thrust, corresponding to approximately 0.5 Nm of torque, based on their location with respect to the center of rotation. This maximum torque can be maintained for several minutes before both the tank pressure and the thruster torques decrease. To show the effects of these thruster torques on the transverse torques, we return to equations (4.14) and (4.15). However, we retain the external torque terms when we substitute the time rate of change of the angular velocities into these equations. We find:

$$g_{r2} = \frac{I_t}{I_2} g_{ex2} + \omega_3\omega_1\left[\frac{I_t(I_3 - I_1)}{I_2} + (I_s - I_t)\right] + \omega_3\omega_s\left[I_s - \frac{I_s I_t}{I_2}\right] \tag{4.46}$$

$$g_{r3} = \frac{I_t}{I_3} g_{ex3} + \omega_2\omega_1\left[\frac{I_t(I_1 - I_2)}{I_3} + (I_t - I_s)\right] + \omega_2\omega_s\left[\frac{I_s I_t}{I_3} - I_s\right] \tag{4.47}$$

Figure 4.16 shows the forces F_2 and F_3 overlayed on plots of ω_3 and ω_2, respectively. We observe once more the connection between the forces and their perpendicular angular velocities. The data in Figure 4.16 is based on a simulation in which we apply a torque about the major axis $\hat{b}_3$. The torque is only applied for thirty seconds. The torque g_{ex3} effectively increases the angular velocity ω_3. This situation is similar to the simple variations in ω_3 that are illustrated in Figures 4.3–4.6. The mean value of the force F_2 increases while the change in amplitude is comparatively smaller. We also notice the effects of g_{ex3} on the frequency of F_3. The frequency of both forces again corresponds to the natural frequency of the system. This relationship is visible for F_3, but less so for F_2 since the amplitude of ω_3 is small.

We describe the effects of the external torques in terms of the amplitude and the frequency of the resulting forces. We individually apply a thirty second torque about each axis and study the effects. Figure 4.17 shows the frequencies of both forces as functions of the external torques. The largest effect on the frequency comes from the external torque about the major axis. The torque g_{ex3} directly increases ω_3. This angular velocity influences the natural frequency of the system, as we see in equation (4.34). The torque g_{ex2} on the other hand has the smallest impact on the overall frequency for both forces.

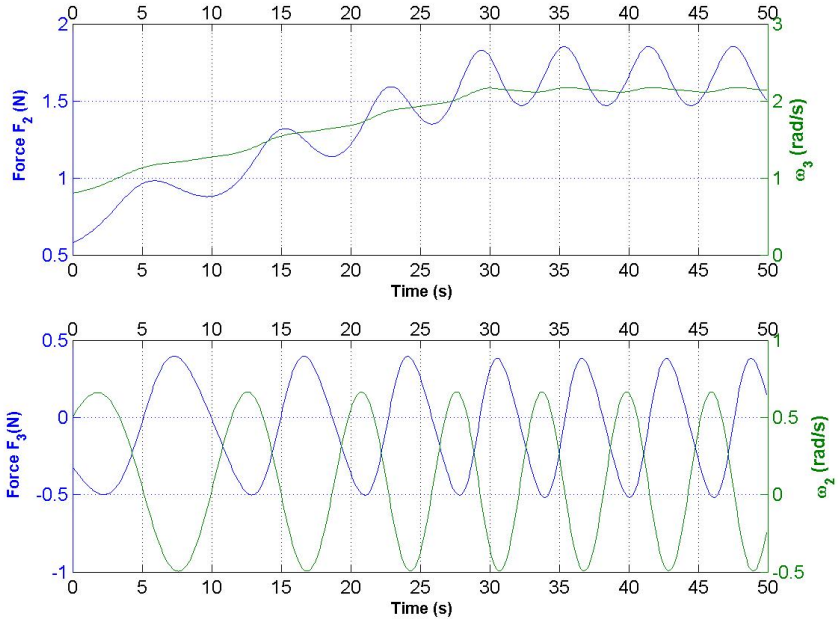

Figure 4.16: *Forces F_2, F_3 and the Angular Velocities ω_3,ω_2 Based on an External Torque g_{ex3}*

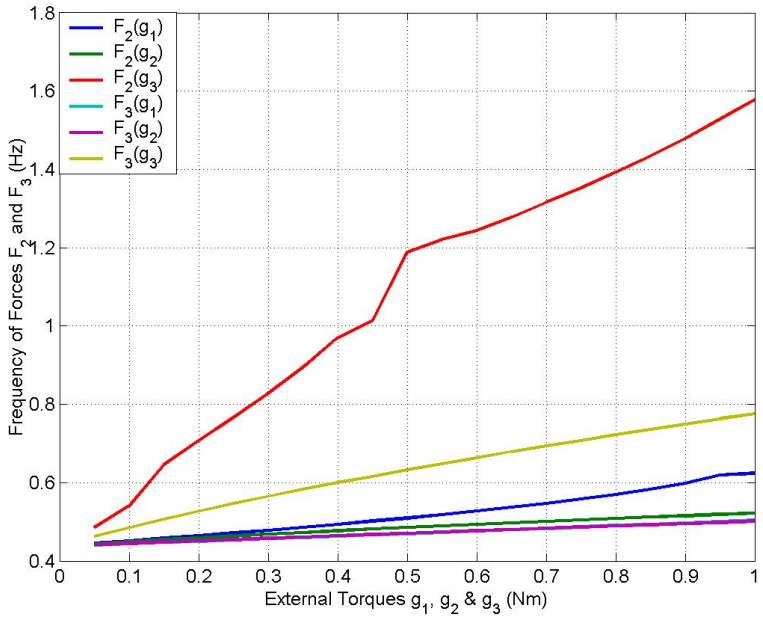

Figure 4.17: *Frequencies of the Forces F_2 and F_3 as Functions of External Torques*

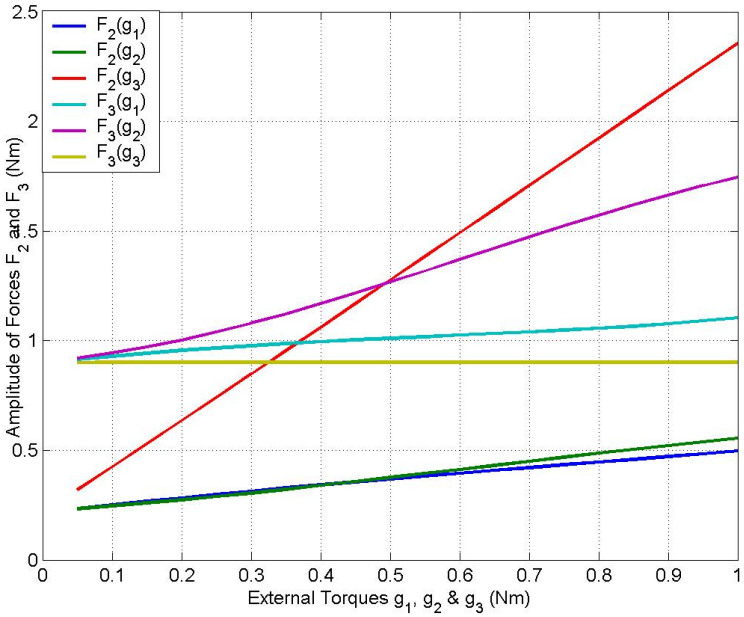

Figure 4.18: *Amplitudes of the Forces F_2 and F_3 as Functions of External Torques*

The amplitudes of the two transverse forces are illustrated in Figure 4.18. Whereas the force F_2 shows a strong dependency on g_{ex3}, we note that the amplitude of F_3 remains constant. Furthermore, both g_{ex1} and g_{ex2} display almost identical effects on F_2 for torques below the nominal value of 0.5 Nm.

Even if we double the nominal external torque, the transverse forces never exceed 2.5 N. This maximum is, of course, dependent on the amount of external torque and the duration over which the torque is applied. However, for Whorl–1, the thrust duration and nominal torque represent reasonable approximations. Thus, we can use these numerical simulations to estimate the force measurements for future experiments.

In this chapter we develop equations for the transverse torques and forces that act on one of the wheels of a multi–wheel gyrostat. We then present a study of these equations in relationship to four different scenarios. First we explore the torque–free gyrostat motion. We then discuss two different attitude maneuvers using momentum wheels. Finally we study the effects of external torques on the gyrostat. The transverse torques are described by equation (4.6). For the specific case of the rotor being aligned with the $\hat{b}_1$ principal axis,

we turn to equations (4.14) and (4.15). These equations show that the transverse torques are proportional to their perpendicular velocities. We conclude, that a steady spin about the rotor's axis produces no internal torques. In addition, the axial torque decouples and does not affect the transverse torques. The rotor geometry also plays an important role. By minimizing the axial inertia we can reduce the magnitude and the frequency of both transverse torques.

Throughout the parameter studies we observe that both torques are functions of the natural frequency of the overall system. We obtain this frequency by linearizing the equations of motion about a desired equilibrium. In general, we observe that within the range of possible motion of Whorl–1 the transverse forces remain small. At twice the nominal conditions the maximum forces have a general upper limit of 3.6 N. We now develop a model of an active magnetic bearing system. With this model we evaluate the performance of magnetic bearings which are subjected to forces described in this chapter.

Chapter 5

Applying the Transverse Torques to a Magnetic Bearing System

There are several different forms of magnetic bearings. Passive magnetic bearings represent the basic implementation of this technology. A single repulsive magnet can levitate the rotor by counteracting the force of gravity. Although very simple, these systems are susceptible to small disturbances and are highly unstable. By positioning several magnets radially around the rotor, we achieve greater stability. However, permanent magnets allow no control over the magnitude of the force in the magnetic field. For this reason, active magnetic bearings use electromagnets as opposed to permanent magnets.

The basic components of an active magnetic bearing system are shown in Figure 5.1. The rotor, sometimes called the target, is suspended in a magnetic field produced by the electromagnets in the stators. The currents for the electromagnets are determined by the controller and regulated by the power amplifier. The controller bases its output on the measurements it receives from the position sensor. In general, there are two electromagnets and two position sensors per degree of freedom. The axes of these components are commonly shifted 45° from the vertical so that no single electromagnet provides the magnetic force to levitate the rotor in a static configuration. Using two magnetic actuators per axis is sometimes referred to as class A control. A single magnetic actuator per axis is called class B control. The Revolve MBRotor kit is considered a class A bearing. Reference [9] provides more details for these classifications.

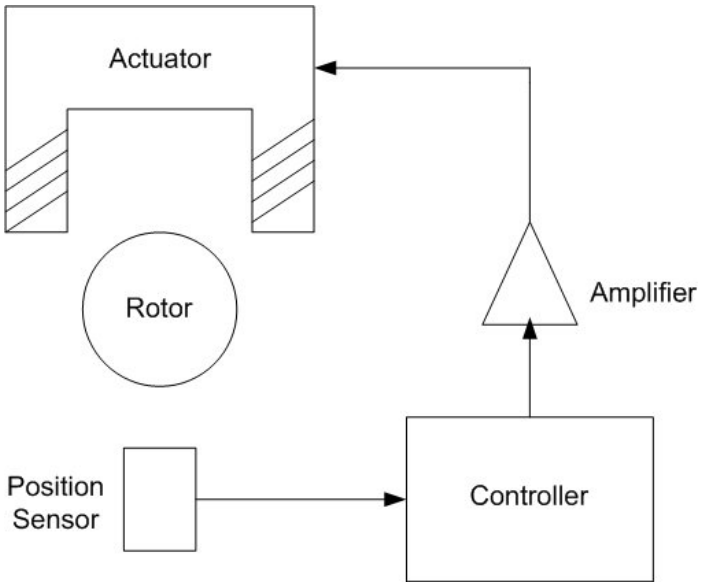

Figure 5.1: *Components of a Magnetic Bearing System*

Allaire *et al*[6] gave a good introduction to the the foundations of designing magnetic bearing systems. A similar useful introduction can be found in reference [7]. Clements[15] developed the equations of motion for a magnetic bearing undergoing base motion and discussed how the process of selecting the gains for a PID controller affects the equivalent stiffness and damping parameters.

In this chapter we introduce the magnetic bearing model and present the related aspects of electromagnetism. We derive the equation of motion of the rotor and discuss the basic controller theory. We consider the peak force limit, the amplifier slew rate and the equivalent stiffness and damping parameters. We then explore the impact of the transverse torques on each of these performance criteria in turn.

5.1 General Model

Like all bearings, magnetic bearings cradle the shaft of rotating machinery. Instead of providing the support through contact forces, the shaft is levitated in a magnetic field. We begin by deriving an expression of the forces created by the magnetic fields in the bearing actuators. We consider a basic bearing model with two opposing magnetic poles for each axis

as seen in Figure 5.2. One quantity to measure a magnetic field is the magnetic induction or magnetic flux density **B**. As a vector, the direction of **B** is tangent to the magnetic field lines. By definition, magnetic field lines originate a magnet's north pole and end at the magnet's south pole. The flux density is proportional to the magnetic field strength **H**:

$$\mathbf{B} = \mu\mathbf{H} \tag{5.1}$$

The permeability μ depends on the material through which the magnetic flux passes. A material's resistance to a magnetic field is called reluctance. For air, the reluctance is small and we use the permeability of free space $\mu_0 = 4\pi \times 10^{-7}[\mathrm{Hm}^{-1}]$.

Magnetic bearings fall under the category of magnetic circuits with air gaps. The magnetic field lines emerge from the stator's north pole, pass through the rotor back to the stator's south pole. The path of these field lines is indicated in Figure 5.2. The flux density B of the magnetic field for one pole of an electromagnet is given by:

$$B = \frac{\mu_0 N I}{2g} \tag{5.2}$$

Here, N refers to the numbers of wire loops in the electromagnet and I is the current provided by the controller. The product of these two quantities is sometimes referred to as the magneto-motive force MMF [7]. The parameter g is a measure of the gap thickness between the rotor and the stator, as seen in Figure 5.2. The magnitude of the attractive force produced in the gaps of one magnet is given by

$$F_g = \frac{\epsilon B^2 A_g}{\mu_0} = \frac{\epsilon \mu_0 N^2 I^2 A_g}{4g^2} \tag{5.3}$$

where A_g refers to the surface area of the magnetic pole, as indicated in Figure 5.2. Since magnetic circuits experience losses due to effects such as fringing and leakage, we can account for these losses via the parameter ϵ. According to [7], ϵ for radial bearings is usually chosen to be 0.8. Since thrust bearings have lower losses, a value of 0.9 for ϵ is commonly chosen.

The phenomenon of fringing occurs only in magnetic circuits with air gaps. At the transition between the metal core and the air, the field lines bulge outward, changing the effective area of the flux path. In magnetic bearing systems, this effect can decrease the magnetic field strength. In other applications, such as tape players, fringing is a necessary part of the design.[5] The term leakage refers to the losses in flux, which are similar to current losses in electrical conductors. The surrounding air has a lower reluctance than the core of an

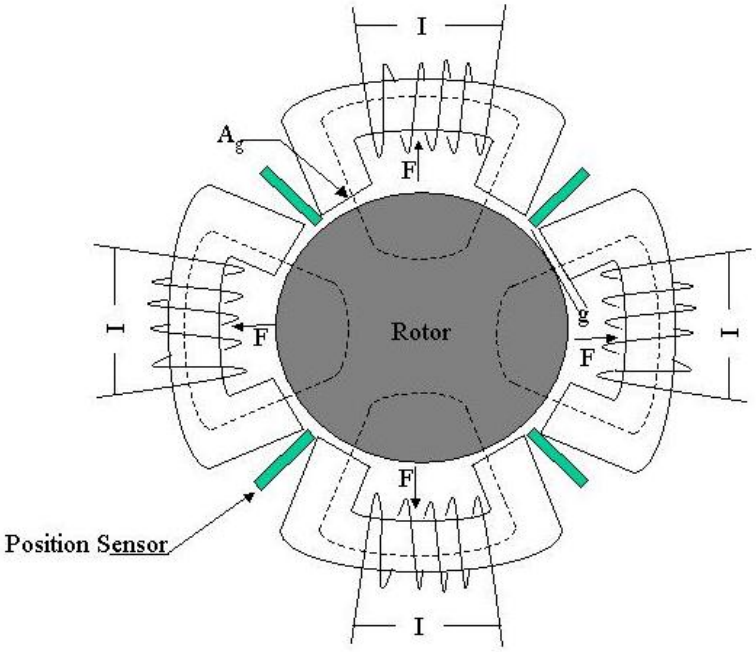

Figure 5.2: *Configuration of a Magnetic Bearing Actuator*

electromagnet and provides an easier path for the magnetic flux. Not all flux lines will therefore remain inside the core, reducing the flux density and the lifting force of the magnet.

In general, the magnetic bearing controller is designed such that the actual coil current I is the sum of a set bias I_B and a perturbation current I_P that is needed to counter shaft displacements. Consequently, there are two corresponding superimposed magnetic fluxes. The flux density B_B of the bias magnetic field, supports the shaft and remains constant unless the bias parameters are changed, whereas the perturbation flux density B_P is time dependent and will vary. Each axis of the bearing actuator consists of two opposing magnets, and each magnet produces an attractive force. The resultant force on the rotor is therefore the difference between the two. Using equation (5.3), we find that the net force on the rotor, expressed in terms of the flux densities, becomes:

$$F_{net} = F_2 - F_1 = \epsilon \frac{A_g}{\mu_0}[(B_{B2} + B_{P2})^2 - (B_{B1} - B_{P1})^2] \tag{5.4}$$

Similar to the coil current, the gap thickness g is composed of a constant and time varying part. Whereas g_0 is the nominal gap thickness between the rotor and the stator, the actual rotor displacement x is a function of time. By substituting in equation (5.2) for the respective

flux densities into equation (5.4), we can rewrite the net force as:

$$F_{net} = \frac{\epsilon \mu_o A_g N^2}{4} \left(\frac{(I_B - I_P)^2}{(g_0 - x)^2} - \frac{(I_B + I_P)^2}{(g_0 + x)^2} \right) \tag{5.5}$$

An added advantage of expressing the coil current I and the gap thickness g in terms of a bias value and a perturbation is the fact that the force equation can now be linearized about the bias conditions. The linear force equation results by truncating a Taylor series expansion of equation (5.5),

$$F_{net} = F_{net}\Big|_{\substack{x=0 \\ I_P=0}} + \frac{\partial F_{net}}{\partial x}\Big|_{\substack{x=0 \\ I_P=0}} x + \frac{\partial F_{net}}{\partial I_P}\Big|_{\substack{x=0 \\ I_P=0}} I_P \tag{5.6}$$

For balanced magnetic bearing systems the first term of equation (5.6) will be zero.[6] We therefore express the linearized force as:

$$F_{net} = K_x x + K_I I_P \tag{5.7}$$

The constants K_x and K_I are referred to as the open loop stiffness and the actuator gain, respectively. Both constants are defined as the partial derivatives of the force F given in equation (5.5). In terms of the bearing properties we can write K_x and K_I as:

$$K_I = \frac{\partial F_{net}}{\partial I_P}\Big|_{\substack{x=0 \\ I_P=0}} = \frac{\epsilon \mu_0 A_g N^2 I_B}{g_0^2} \tag{5.8}$$

$$K_x = \frac{\partial F_{net}}{\partial x}\Big|_{\substack{x=0 \\ I_P=0}} = -\frac{\epsilon \mu_0 A_g N^2 I_B^2}{g_0^3} \tag{5.9}$$

We note that the open loop stiffness is always negative, making the magnetic bearing system inherently unstable. As the rotor moves closer to one of the electromagnets, the attractive force increases, requiring the controller to adjust the currents in both magnets to keep the shaft position stable. We can write the equation of motion of the rotor, in a one degree–of–freedom case, as:

$$M_R \ddot{x} + K_x x + K_I I_P = F_{ex} \tag{5.10}$$

The external force F_{ex} itself has two components. While the platform remains stationary, the force in magnetic field only supports the weight of the rotor. The levitation of the

rotor is maintained by a static force F_{stat}, which requires an associated current I_{stat}. As the platform begins to rotate, a dynamic force F_{dyn} is induced due to the transverse torques between the platform and the rotor. The corresponding current I_{dyn} is required to counteract these dynamic forces and to keep the rotor centered. The total external force on the rotor is therefore:

$$F_{ex} = F_{stat} + F_{dyn} \tag{5.11}$$

As we see from equations (4.16) and (4.17), the dynamic forces are functions of the angular velocities of the platform P and the relative angular velocity of the rotor. We explore this relationship further in Section 5.4.

5.2 Controller

Since the open loop magnetic actuator is unstable, a controller is an integral part of a magnetic bearing system. Based on shaft position, the controller determines the appropriate currents for each electromagnet. Figure 5.3 shows the block diagram of the overall bearing system. We can express the controller transfer function as:

$$G(s) = \frac{I_P(s)}{x(s)} \quad \longrightarrow \quad I_P(s) = G(s)x(s) \tag{5.12}$$

Taking the Laplace transform of equation (5.10) and substituting in $I_P(s)$ from equation (5.12) above we obtain the transfer function of the overall bearing system:

$$\frac{x(s)}{F(s)} = \frac{1}{M_r s^2 + K_x + K_I G(s)} \tag{5.13}$$

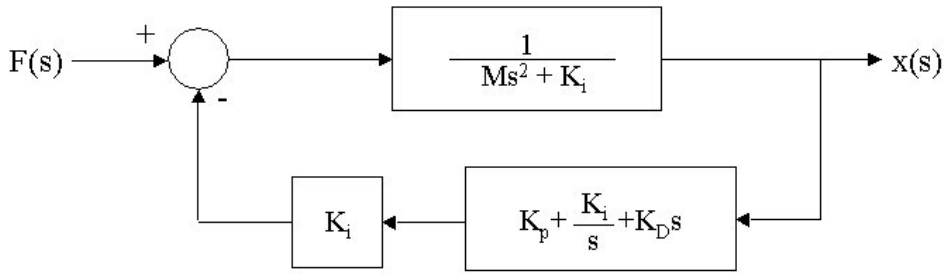

Figure 5.3: *Block Diagram of the Basic Magnetic Bearing Control System*

There are several elements to the controller that are described by the transfer function $G(s)$. Referring to Figure 5.1, these elements consist of the position sensor, the power amplifier and the controller itself. The first two of these elements are in essence fixed and cannot easily be adjusted. They both, however, influence the overall controller performance. Alliare[7] gives first–order transfer functions for both the position sensor and the power amplifier:

$$\text{Sensor} \Leftrightarrow \frac{V_s(s)}{x(s)} = \frac{K_s}{1+\tau_s s} \quad \text{Amplifier} \Leftrightarrow \frac{I_P(s)}{V_c(s)} = \frac{K_a}{1+\tau_a s}$$

Each of these devices has a transfer function that contains gains, K_s and K_a, as well as time constants τ_s and τ_a. These parameters are generally fixed and can not be modified. The controller element from Figure 5.1, contains the electronic control law implementation. The exact nature of the control law depends on the individual design. Proportional-Integral-Derivative (PID) controllers are the most often discussed in magnetic bearing literature. The transfer function for this controller is given by:

$$G_c(s) = K_t\big(K_p + \frac{K_i}{s} + K_d s\big) \tag{5.14}$$

The proportional gain K_p is similar to a stiffness constant and the derivative gain K_d acts like a damping term. The integral gain K_i is associated with the lower frequency centering of the rotor, and eliminates steady–state errors. We also include a total gain K_t, which multiplies the entire transfer function. This total gain can be used to further tune the overall gains. Including the sensors and the amplifier, the general transfer function $G(s)$ then becomes:

$$G(s) = \frac{K_t K_s}{1+\tau_s s}\left(K_p + \frac{K_i}{s} + K_d s\right)\frac{K_a}{1+\tau_a s} \tag{5.15}$$

Other types of controllers can be substituted for the PID controller, depending on the desired effects we would like to achieve.

Once all the various gains have been selected, we have sufficient information for the closed loop system expressed in equation (5.13). The interaction of the bearing actuator and the controller contribute to the equivalent stiffness and damping of the system. We therefore can incorporate these effects and model the overall active magnetic bearing as a mass-spring-damper system, much like conventional bearings. Clements[15] gave a derivation of equivalent stiffness K_{eq} and damping C_{eq} which we discuss in section 5.5.

5.3 Peak Force Limit

A fundamental property of the ferromagnetic materials often used in electromagnets is the saturation limit of the magnetization. Once this limit is reached, any increase in flux only leads to small increases in the magneto–motive force. In other words, even if greater and greater currents are applied to the electromagnet of a magnetic bearing, the attractive force increases only slightly and the shaft's motion can no longer be controlled. Plonus[5] gave a good explanation of magnetization for various materials and described the saturation phenomenon in detail. We return to equation (5.1):

$$B = \mu_0 H \quad \text{where} \quad H = \frac{NI}{2g} \tag{5.16}$$

Here the quantity H is the magnetic field strength or intensity. For ferromagnetic materials, such as the silicon-iron used in the MBRotor Kit, equation (5.16) describes only the linear portion of the actual relationship between the flux density and the field intensities. Outside of this linear region, the flux density levels off and eventually reaches a maximum value. Figure 5.4 is a qualitative graph of this behavior. The flux density at which saturation occurs is commonly referred to as B_{sat}. The maximum force that is generated in one gap of a magnetic bearing, is given by:

$$F_{max} = \frac{\epsilon B_{sat}^2 A_g}{2\mu_0} = \frac{\epsilon \mu_0 N^2 I_{sat}^2 A_g}{4g^2} \tag{5.17}$$

Thus we can achieve higher values of the maximum attractive force F_{max} either by increasing the size of the cross-sectional pole area A_g, since μ_0 is a constant, or by choosing different materials which have a higher saturation flux density. Table 9.2 in Plonus[5] gives an overview of the saturation flux densities for several commonly used materials. The values of B_{sat} range from 0.32 and 2.4 Wb/m^2. We note that the overall design choices here are limited. Therefore, increasing the bearing geometry is the simplest way to increase the maximum load of a magnetic bearing. The MBRotor manual indicates that the radial bearing magnets are made from silicon-iron. Plonus lists three different types of silicon-iron, with values for B_{sat} of 1.95, 2.0 and 2.01 Wb/m^2. By using the first form of equation (5.17), with the radial bearing data listed in Table B, we can recalculate the force at saturation given in the Figure 5.5. We find that with a saturation flux density of about 1.95 Wb/m^2, we match the maximum force value given in the graph. A similar calculation can be made for the thrust bearing. Here we find a B_{sat} of 1.41 Wb/m^2. The material of the thrust bearing is

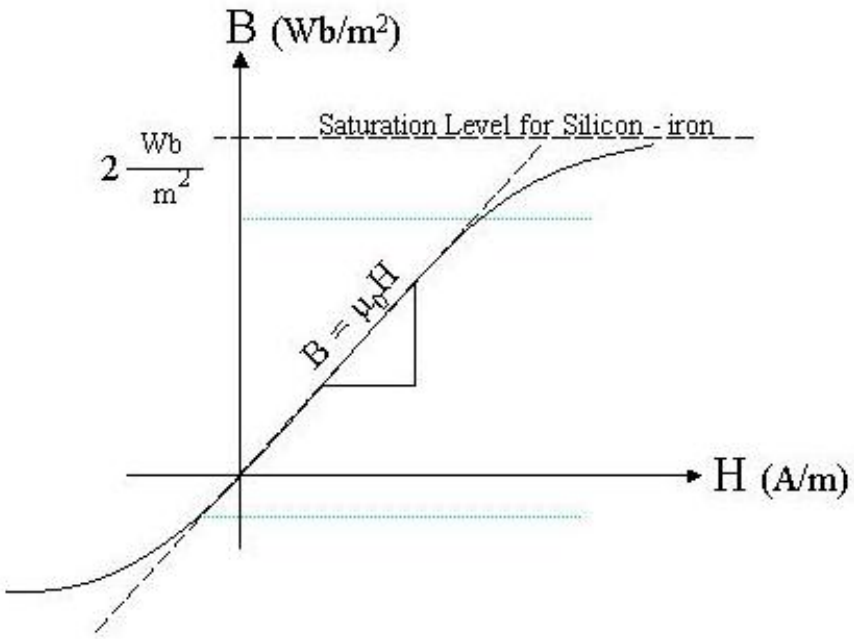

Figure 5.4: *Qualitative Representation of the B–H Relationship for Ferromagnetic Materials*

listed as 410-SS in the MBRotor kit manual, but no saturation flux density was listed in reference [5]. An alternative method to determine the maximum available force for a given magnetic bearing is to use the second form of equation (5.17). However, here we require the knowledge of both the final gap size as well as the saturation current. Both these parameters are readily available during the operation of the magnetic bearing system, since the gap size is the measured input to the controller and the current is the controller output.

Depending on the design, it is possible that the poles of the magnets have either an angled or curved surface. This seems especially common with rotating machinery, where the poles are in close proximity to a round shaft. In this case, the projected pole area A_p and the actual pole area A_g are frequently treated separately. The distinction between the two parameters is highlighted in Figure 5.6. Maslen *et al*[8] derived an expression for the maximum force that incorporates both areas:

$$F_{max} = \frac{\epsilon B^2 A_p^2}{\mu_0 A_g} \tag{5.18}$$

The Revolve MBRotor kit uses poles that are designed with a flat pole surface, where both the projected and actual pole areas are equal to each other, in which case equation (5.18) reduces back to equation (5.17).

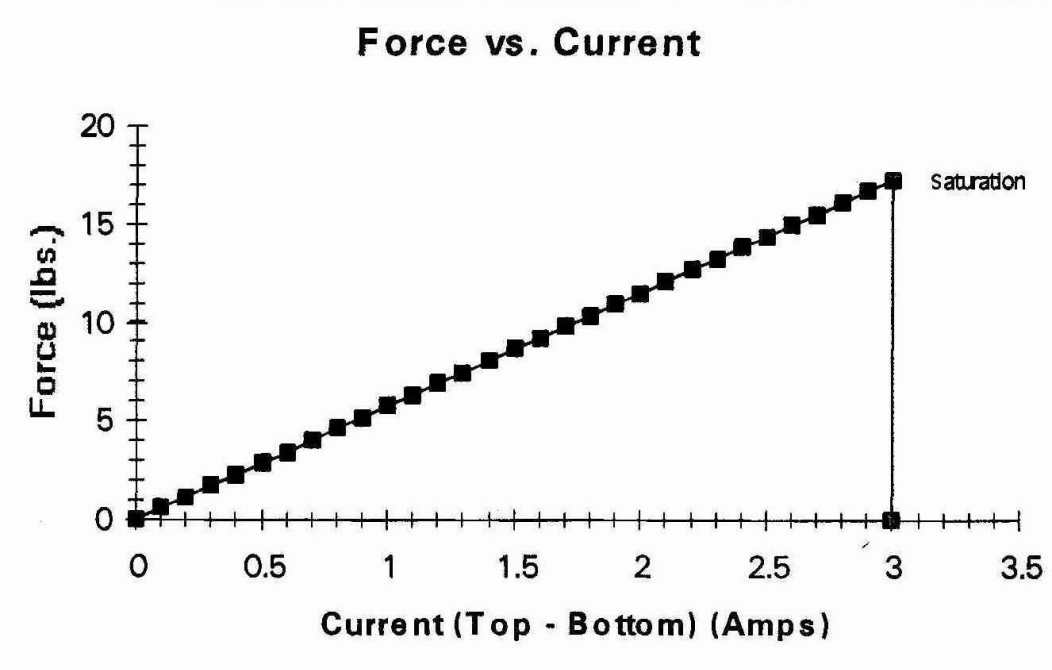

Figure 5.5: *Force vs. Current Graph of the Revolve Radial Magnetic Bearing*

The magnetic bearings are required to generate a force that is sufficient to overcome both a static and dynamic load. The static load is simply the force due to gravity on the rotor. The dynamic load is the additional force that arises from other sources, such as imbalance, forced excitation or base motion. Therefore, for a given rotational maneuver, the sum of the static and dynamic forces in the bearing cannot exceed F_{max}. If this situation occurs, the controller will no longer be able to compensate for the forces and the rotor's displacement will become unstable. The controller then triggers an alarm based on a preset maximum displacement, and the system comes to a halt. Most active magnetic bearings contain an anti–friction backup bearing. This backup bearing supports the shaft as it delevitates. To provide the largest current range, a common recommendation is to set the bias current level at $I_{sat}/2$, where I_{sat} is the current associated with the saturation flux density and therefore with the maximum force. Incidentally, the saturation current is also the set point about which equation (5.5) is linearized.

Figure 5.5 shows a graph of the bearing force as a function of the applied current. This graph represents the specifications of the radial bearings, and is taken from the MBRotor Kit manual[12]. According to this graph, the radial bearings reach saturation at 3 Amps

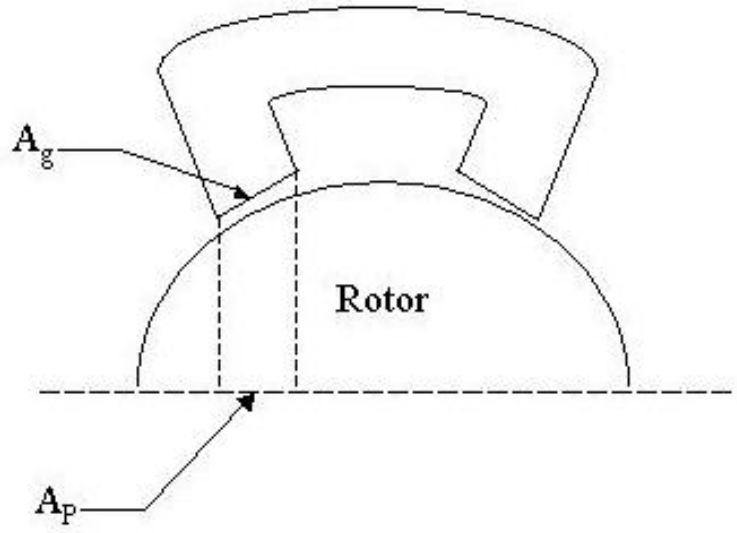

Figure 5.6: *Difference between the Gap Area A_g and the Projected Area A_P*

with a F_{max} of 17 lbf (75.62 N). This graph defines the limits of the forces the magnetic bearing can experience. It therefore provides a baseline at which we can compare the forces resulting from the transverse torques. If we consider a bearing configuration with a 18 in shaft, a 1/2 in and a 1/4 in balance disk, the total weight of the rotor is 1.582 kg. This rotor generates a static load of 15.52 N on the radial bearings. The upper limit of the dynamic load becomes 60.1 N or 30.05 N per bearing.

Based on the study of the transverse torques in Chapter 4, we comment on the effects of the internal forces on the saturation limit of this magnetic bearing configuration. Returning to the results from the individual cases we discuss in Sections 4.2 through 4.4, we now justify the earlier qualitative statement regarding the relative size of the obtained forces. Throughout the discussed cases, we find that the maximum values for F_2 and F_3 remain below 3.55 N. For the nominal case, the peak force values remain below 2 N. We conclude that, the internal forces only achieve 6% of their allowable maximum values. As a result, the transverse torques do not reach the peak force limit.

For the estimated range of motion of Whorl–1, the transverse forces remain below the peak force limit. However, there are situations that can cause the internal forces to exceed this limit. If Whorl–1 tilts passed the 5° limit, its surface hits the air bearing cup. The resulting impulsive force could lead to a position alarm of the magnetic bearing. These alarms are

triggered if the rotor moves outside a preset limit. The purpose of this limit is to protect both the electromagnets and the position sensors in the stator. Usually this limit coincides with the inner diameter of the back–up bearing. Of course, we can also modify either the rotor or Whorl–1 to operate outside of the nominal range of motion. For example, by increasing the weight of the rotor, we reduce the possible range of any dynamic loads. Other possibilities include changing the bias settings. The bias current is usually set at one half the maximum value. Increasing the bias current reduces the possible range of control current. Adjusting the center position achieves similar results. Moving the rotor closer to one side of the stator decreases the range of dynamic forces because the two opposing electromagnets no longer apply an equal amount of force to shaft. The effects of a bearing shutdown during normal operation are worth exploring since the sudden change in axial angular momentum of the rotor requires a quick response from the overall attitude controller.

5.4 Force Slew Rate

The second performance limit we discuss is the force slew rate. It quantifies how fast an active magnetic bearing system responds to changes in the required force. The maximum slew rate is found by differentiating either equation (5.5) or (5.7) with respect to time, while keeping the rotor displacement x equal to zero. Bornstein[9] developed an expression using equation (5.5). Given a sinusoidal external force $F_{dyn} = F\sin(\omega_F t)$, the maximum force slew rate is:

$$F_{dyn} = \frac{I_B V_p A_f}{2g\omega_F} \tag{5.19}$$

Here V_p is the peak voltage of the power amplifier and A_f is the ratio of the magnetic projected area to the total inductive area. For electromagnets with a straight pole design, A_f is either equal or close to unity. Both Maslen *et al*[8] and Siegwart *et al*[10] derived similar expressions to describe the limit to the force slew rate. Although these three results are valid under different conditions, all three include essentially the same parameters. All three are functions of the peak amplifier voltage and the gap geometry. Whereas both Siegwart *et al* and Bornstein's expressions dealt with a sinusoidal excitation force, Maslen *et al* only derived a generalized inequality. The amplifier slew rate limit has two main effects. The first effect is that the actuators in the magnetic bearings will cause a phase lag. The electromagnets are no longer able to respond to the control signal quickly enough. This effect leads to a loss of damping in the system. Secondly, the applied and demanded current in the magnetic

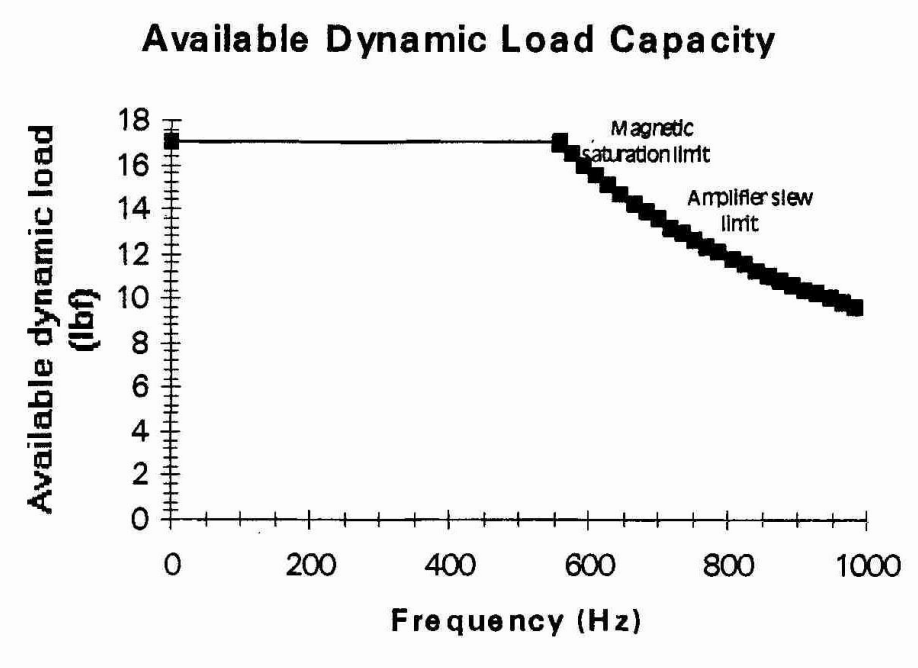

Figure 5.7: *Force vs. Frequency Graph of the Revolve Radial Magnetic Bearing*

bearing circuits will become further distorted, which will ultimately result in a further loss of stiffness and damping [8].

The amplifier slew rate for the radial bearings of the MBRotor kit is shown in Figure 5.7[12]. The graph, taken from the MBRotor kit manual, shows the maximum available force as a function of the frequency of a cyclical input force. The data are not based on calculations using equation (5.19), but on empirical measurements. For the radial bearings, the magnetic saturation sets in at 17 lbf (75.62 N) at roughly 550 Hz.

It is apparent that we need to quantify the frequency of the forces F_2 and F_3 in order to make use of equation (5.19). As discussed in Chapter 4, the forces caused by the rotational motion of the platform are proportional to the angular velocities of the overall system. In fact, when considering a torque–free case the frequency of oscillation of both forces is the natural frequency of the gyrostat's motion. We recast equation (4.34) for clarity:

$$\omega_n = I_n \Omega \qquad \text{where} \qquad I_n = \sqrt{\frac{(I_3 - I_2)(I_3 - I_1 + I_s)}{I_2(I_1 - I_s)}} \tag{5.20}$$

We estimate the maximum for the angular velocity Ω of Whorl–1 to be 0.8 rad/s, or

0.1273 Hz. At this speed, the natural frequency ω_n becomes 0.059 Hz. Even if we double the maximum value of Ω, we find a natural frequency of 0.118 Hz. These frequencies are generally small and the dynamic load capacity of the MBRotor kit is effected. Active magnetic bearings are designed to operate with unbalanced rotors. The cyclical forces generated by an imbalance are proportional to the angular velocity of the rotor. We find that even a small imbalance has a larger effect on the amplifier slew limit than the cyclical forces caused by base motion.

5.5 Stiffness, Damping and Natural Frequency

Besides the peak force limit and the amplifier slew rate, the transverse torques could also affect the stiffness and damping parameters of an active magnetic bearing system. To analyze these effects, we develop an equivalent Jeffcott Rotor model. This simplified model provides the basis for many rotordynamic texts such as Erich[24] and others. A good introduction can also be found in the class notes by Leader.[25] The Jeffcott rotor consists of a shaft with a balance disk supported by two bearings. Since the bearings provide both stiffness and damping, the equation of motion of the shaft is given by the well–known equation for a mass–spring–damper system:

$$M\ddot{x} + C\dot{x} + Kx = F_{forcing function} \tag{5.21}$$

In most cases the forcing function is harmonic. Examples of harmonic forcing functions include unbalance forces, bowed shafts and misaligned disks. We recall that for the torque-free case discussed in Section 4.2, the forces generated by the rotational motion are cyclical. However, all forces thus far have been expressed in the rotating reference frame $\mathcal{F}_{\mathcal{B}}$. These forces are responsible for keeping the rotor's motion in accordance with the motion of the platform. To understand the effects these forces have on the stiffness and damping of the magnetic bearings, we assume that we are applying equivalent forces to a stationary bearing system. First, we derive expressions in terms of the components of a magnetic bearing rotor system that allow the overall equations of motion of the rotor to be written in the form given by (5.21). Once developed, we use these expressions to evaluate the stiffness and damping as well as the natural frequency of the rotor system under the effects of the forces generated by the rotational motion.

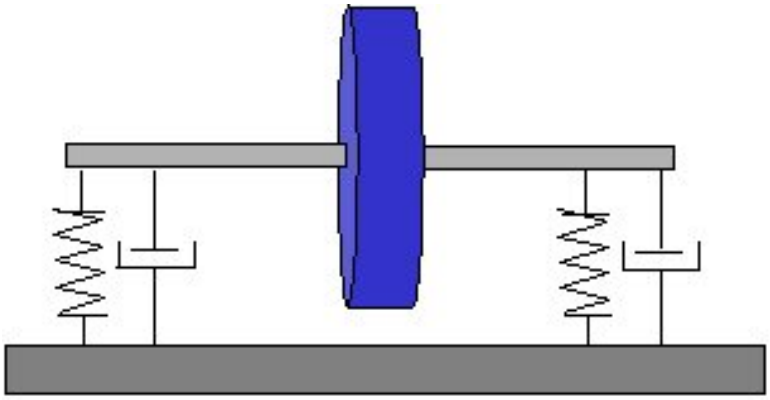

Figure 5.8: *Jeffcott Rotor – a Simplified Model*

As described in Section 5.2, the field strengths of the magnetic bearings are determined by a feedback control system. The controller also influences the stiffness and damping characteristics of the overall bearing. As shown in equation (5.12), the transfer function of the controller relates the required perturbation current I_P to the shaft's position. Replacing I_P in equation (5.10) with the transfer function we arrive at an expression similar to (5.13):

$$\big(M_r s^2 + K_x + K_I G(s)\big)x(s) = F_{ex}(s) \tag{5.22}$$

For harmonic input forces, the transfer function $G(s)$ will relate information about the amplitude and the phase of the output signal. We can therefore express $G(s)$ as a complex valued function:

$$G(j\omega) = Re_G(\omega) + jIm_G(\omega) \tag{5.23}$$

Similarly, evaluating equation (5.22) at the input frequency we find:

$$\big(- M_r\omega^2 + K_x + K_I(Re_G + jIm_G)\big)x(j\omega) = F_{ex}(j\omega) \tag{5.24}$$

The stiffness and damping terms in (5.24) are a mixture of the open loop stiffness, actuator gain and the components of the complex representation of the transfer function. To sort out the respective terms we define equivalent stiffness K_{eq} and equivalent damping C_{eq} parameters. We equate these new parameters with the relevant components of equation (5.24):

$$(K_{eq} + C_{eq}j\omega)x = (K_x + K_I(Re_G + jIm_G))x \tag{5.25}$$

We simply collect the real and imaginary values on the right side of the equation and find:

$$K_{eq} = K_x + K_I Re_G \tag{5.26}$$

$$C_{eq} = \frac{K_I Im_G}{\omega} \tag{5.27}$$

The composition of the real and imaginary components depends on the type of implemented controller. The open–loop magnetic bearing consists of a mass–spring system with a large negative stiffness. This system is unstable and does not contain any energy dissipation. As a result the system requires a controller to overcome the negative stiffness and provide damping to the system.

Most active magnetic bearings implement a PID–controller. Substituting (5.14) into equation (5.22) and multiplying both sides of the equation by s, we find:

$$\left[s^3 + \frac{K_d K_I}{M_r} s^2 + \frac{K_x + K_I K_p}{M_r} s + \frac{K_i K_I}{M_r}\right] x(s) = \frac{s F_{ex}(s)}{M_r} \tag{5.28}$$

In this approach we are not including the sensor and amplifier dynamics. Furthermore we set the total gain $K_t = 1$. We observe that the integral term of the PID controller introduces a zero and a third pole. The Jeffcott model, as given by equation (5.21), is a second order system. We reconcile this difference by expressing (5.28) as a factored polynomial:

$$(s + p_1)\left(s^2 + \left(\frac{K_d K_I}{M_r} - p_1\right) s + \left(\frac{K_x + K_I K_p}{M_r} - p_1 \frac{K_d K_I}{M_r} + p_1^2\right)\right) x(s) = \frac{s F_{ex}(s)}{M_r} \tag{5.29}$$

For good closed–loop performance, a third order transfer function generally has a single real pole and a complex conjugate pair. In equation (5.29), p_1 refers to the real pole. To guarantee stability, all three poles need to be in the left–half portion of the complex plane. Furthermore, the distance of the pole to the imaginary axis is inversely proportional to the time constant. By choosing a large negative p_1, the effects of this pole on the dynamics of the system become short–lived. We then use the remaining second order system to discuss the equivalent stiffness and damping terms.

Using a state space pole placement method we determine the gains for the PID controller by specifying a desired set of poles. Choosing these gains introduces an entire new sensitivity study. The emphasis of this study is on the effects of base motion. We therefore choose gains that provide stability and not necessarily the optimal performance or lowest control effort.

To find appropriate gains, we express the equations of motion in state space form:

$$\begin{bmatrix} \dot{x}_1 \\ \dot{x}_2 \\ \dot{x}_3 \end{bmatrix} = \begin{bmatrix} 0 & 1 & 0 \\ 0 & 0 & 1 \\ 0 & \frac{-K_x}{M_r} & 0 \end{bmatrix} \begin{bmatrix} x_1 \\ x_2 \\ x_3 \end{bmatrix} + \begin{bmatrix} 0 \\ 0 \\ \frac{1}{M_m} \end{bmatrix} \mathbf{u}(t) \tag{5.30}$$

Equation (5.30) represents the augmented state equations. To implement an integral controller, we define an additional state x_1 which represents the integral of the shaft's position. The state space version of a PID controller is a simple state feedback controller with the appropriate gains. We determine the gains by choosing poles with negative real parts. One such set of poles is $(-50, -5-5j, -5+5j)$. The resulting gains are:

$$\begin{aligned} K_t &= 1 \\ K_p &= 2.2837 \times 10^7 \\ K_i &= 55.068 \\ K_d &= 1.3216 \end{aligned}$$

We note the large value of the proportional gain. The open–loop stiffness K_x of the MBRotor kit is 22,836,010 N/m. The difference between K_x and K_p is 990 N/m. With these gains, the closed–loop system is guaranteed to be stable.

Returning to the transfer function, we express the real and imaginary components in terms of the controller gains:

$$Re_G = \left(\frac{K_x + K_I K_p}{M_r} - p_1 \frac{K_d K_I}{M_r} + p_1^2 \right) \tag{5.31}$$

$$Im_G = \left(\frac{K_d K_I}{M_r} - p_1 \right) \omega \tag{5.32}$$

For the PID–controller, the real part of the transfer function, and therefore K_{eq} is independent of the frequency. The equivalent stiffness is a constant. Similarly the equivalent damping C_{eq} is also constant based on equations (5.32) and (5.27). Both parameters become:

$$K_{eq} = K_x + K_I \left(\frac{K_x + K_I K_p}{M_r} - p_1 \frac{K_d K_I}{M_r} + p_1^2 \right) \tag{5.33}$$

$$C_{eq} = K_I \left(\frac{K_d K_I}{M_r} - p_1 \right) \tag{5.34}$$

It is important to note, that both K_{eq} and C_{eq} represent the stiffness and damping parameters of the magnetic bearing system once the transient effects of the third pole have subsided.

Furthermore both parameters are now functions of the pole p_1. This real pole is introduced by including an integral component in the control law. There is also a direct relation between the magnitude of the integral gain, and the location of the pole in the complex plane. A smaller integral gain K_i moves p_1 closer to the imaginary axis. Setting $p_1 = 0$, equation (5.29) becomes:

$$\left(s^2 + \frac{K_d K_I}{M_r} s + \frac{K_x + K_I K_p}{M_r}\right) x(s) = \frac{F_{ex}(s)}{M_r} \tag{5.35}$$

In this case we see that the damping and stiffness coefficients of this second order equation are directly related to the derivative and proportional gains, respectively. Similarly, K_{eq} and C_{eq} become functions of their respective gains.

$$K_{eq} = \frac{K_x + K_I K_p}{M_r} \tag{5.36}$$

$$C_{eq} = \frac{K_d K_I^2}{M_r} \tag{5.37}$$

As we increase the integral gain, thus moving p_1 further left in the complex plane, both the stiffness and damping change. For large values of p_1 the integral gain dominates the dynamics, which can lead to an unstable closed–loop system.

Thus far we have accounted for the damping and stiffness effects of the controller and the magnetic field. The remaining element that is left to model is the flexibility of the shaft. Even though most shafts are made out of materials such as stainless steel, they are not rigid and have an inherent stiffness. For circular shafts, this stiffness can be calculated by the following equation:

$$k_{shaft} = \frac{48EI}{L^3} \tag{5.38}$$

Here, E refers to the Youngs' modulus or modulus of elasticity, which is a material dependent property. The shaft's length is denoted by L. The inertia parameter I is a function of the shaft's diameter d and is determined by:

$$I = \frac{\pi d^4}{64} \tag{5.39}$$

According to Leader,[25] we can now write the stiffness of the entire magnetic bearing–rotor system as:

$$\frac{1}{K_{sys}} = \frac{1}{2k_{eq}} + \frac{1}{k_{shaft}} \tag{5.40}$$

Since the shaft does not add any damping, the overall system damping is given by C_{eq}.

$$C_{sys} = \frac{K_d K_I}{M_r} - p_1 \tag{5.41}$$

To complete this analysis in terms of the Jeffcott rotor model, we introduce the concept of the modal mass M_m. There are several methods in rotor dynamics to estimate the portion of the rotor's mass that is most influential to the overall response. Leader[25] defined the modal mass to be the effective mass that contributes to a rotor's displacement as it passes through one of the system's critical speeds, or modes. The modal mass is based on the assumption that the entire mass is located at the midspan of the rotor. As such, the ratio of the bearing to the shaft stiffness is an important factor. For "stiffer" bearings, the response of the shaft at the critical speeds becomes less dependent on the stiffness of the shaft. On the other hand, as the bearing stiffness decreases, the rotor will act more and more like a rigid body, and the modal mass will become increasingly equal to the total mass of the rotor. The range of the modal mass to total mass ratios is commonly between 0.55 and 0.65. A ratio of 0.6 is recommended as an average value for basic analytic purposes.

We now have all the parameters to describe the Jeffcott model in terms of the magnetic bearing system. The overall stiffness and damping parameters of the system are given by:

$$K_{sys} = \frac{2K_{shaft}\left(\frac{K_x+K_IK_p}{M_m} - p_1\frac{K_dK_I}{M_m} + p_1^2\right)}{K_{shaft} + 2\left(\frac{K_x+K_IK_p}{M_m} + p_1\frac{K_dK_I}{M_m} + p_1^2\right)} \tag{5.42}$$

$$C_{sys} = \frac{K_IK_d}{M_m} - p_1 \tag{5.43}$$

We observe that both the stiffness and damping are not affected by the frequency of the input force. This simplified Jeffcott rotor model, with a PID controller, shows that the transverse torques have no effect on the stiffness and damping of the active magnetic bearing system. Since this result largely depends on the implemented controller, we can not conclude that these results are true for all cases. In addition to the sensor and amplifier dynamics, Clements[15] also included a low pass and a notch filter in the overall transfer function. His results showed a frequency dependency for both stiffness and damping. However, these effects occurred at frequencies above 1Hz, which is the upper limit of the frequency range of the transverse torques.

The most common disturbance forces acting on rotating machinery are caused by imbalances or bowed shafts. These forces are functions of the rotational speed of the rotor. An unbalance force, for example, is calculated by:

$$F_{unbalance} = mr\omega_r^2 \tag{5.44}$$

Here ω_r is the rotational speed of the rotor. Imbalances are commonly measured as oz-

in, represented by the parameter mr. A one oz-in unbalance at 3600 rpm, for example, produces a force of 23.01 lbf (102.35 N). Active magnetic bearings are sized to compensate for these kinds of forces. The forces generated by the rotational motion of the platform are comparatively small. The performance of a nominally operating active magnetic bearing should not be affected by these internal forces. However, by modifying the rotor system we bring it closer to its limitations. By increasing the weight of the rotor, we reduce the range of possible dynamic forces. Thus the bearing operates closer to its peak force limit. Similar effects result from changes made to the bias current or bias positions. Another possibility is to modify the gains of the controller and make the magnetic bearing system marginally stable. Finally, modifications to Whorl–1 could also be made. The transverse torques are proportional to the angular velocities of the platform. Operating Whorl–1 outside of the estimated range increases both the frequency and amplitude of the transverse torques. In the near future, we intend to investigate these and other possibilities.

Chapter 6

Conclusions

There are an increasing number of proposed applications for active magnetic bearings in spacecraft design. Magnetic bearings have been used to support reaction wheels on several satellites of the SPOT series. Other suggested applications include rate sensing and energy–storing flywheels. The rotational motion of the spacecraft will generate torques between the rotating machinery and spacecraft structure. The forces resulting from these torques potentially affect the performance of active magnetic bearings.

Based on the gyrostat model we develop an expression of the transverse torques. These torques act on one wheel of a multi–wheel gyrostat. These torques, expressed in a body–fixed frame, are functions of the angular velocities of the gyrostat. Based on a parameter study, we draw two conclusions. If the rotor's spin axis is aligned with one of the principal axes, the axial rotor torque g_a decouples from the two transverse torques. Also, if the platform is in a stable motion about the rotor's spin axis the transverse torques become zero.

The shape of the rotor also affects the magnitudes and the frequency of the internal torques. By minimizing the axial inertia of the rotor, both transverse torques decrease. The derived equation can therefore be used in designing a rotor for systems that operate near the performance limits of the bearings.

We evaluate the transverse torque equation based on the nominal motion of the Distributed Spacecraft Attitude Control Systems Simulator (DSACSS), also dubbed Whorl–1. The magnetic bearing is modeled after the Revolve MBRotor kit. We assume the spin axis of the

magnetic bearing is parallel to the minor axis of Whorl–1.

For this system we define the nominal range of motion. Within this range, we discuss a torque–free motion, a 90° slew maneuver, a steady spin maneuver and motion with external torques. Studying the effects of parameters of the gyrostat, we note that the frequency of the internal torques is equal to the natural frequency of the gyrostat. The magnitudes of the forces remain small. The largest force we encounter is 3.6 N for F_2 during the 90° slew maneuver.

We then introduce an active magnetic bearing model implementing a Proportional–Integral–Derivative controller. The equation of motion of the rotor in the magnetic field can be linearized about the bias settings. For active magnetic bearings, each axis is treated separately. The coupling effects are commonly neglected. The linearized equations represent a simple mass–spring system. Since the open–loop stiffness is negative, the system is unstable. The applied controller provides a closed–loop stable system with positive stiffness and damping.

Magnetic bearings are subject to performance limitations. We discuss the peak force limit, the amplifier slew limit, and the closed–loop stiffness and damping values based on an equivalent Jeffcott rotor analysis. The estimated range of motion of the DSACSS system does not result in forces that exceed these performance limits for the MBRotor magnetic bearing. The magnitudes of the forces amount to less than 6% of the maximum dynamic load capacity. In addition, the low frequencies of the cyclical forces remain several orders of magnitudes below the amplifier slew limit. We observe that the Jeffcott rotor analysis ,implementing a PID controller, shows that both the system's stiffness and damping are constant, and thus not affected by the input forces due to the rotational motion.

Possible modifications to the DSACSS-MBRotor gyrostat are also introduced. Of the discussed performance limits, the peak force is the most critical. Increasing the rotor mass or changing the current or position bias settings reduces the allowable dynamic force range. The magnetic bearing is driven closer to its peak force limitations. Once the DSACSS–MBRotor test bed becomes fully operational, we will continue the investigation of the effect of base motion on active magnetic bearings.

Appendix A

Distributed Spacecraft Attitude Control System Simulator (DSACSS)

In this section we present the Distributed Spacecraft Attitude Control System Simulator (DSACSS). We use this simulator, otherwise known as Whorl–1, as the rotating platform. Whorl–1 consists of an aluminum honeycomb lower deck that is mounted on a hemispherical air bearing. The air bearing supports a total weight of 300 lb. The entire assembly resembles a table–top. Whorl–1 is free to spin about its major axis and can tilt up to 5° in both transverse axes. The lower deck contains all the components necessary for Whorl–1's operation. These components include the onboard computer, rate sensors, wireless ethernet card, three momentum wheels, a gas thruster system, batteries and three linear actuators. In addition to these standard components, a control–moment–gyro assembly can be attached to the lower deck as well. The upper deck of Whorl–1 is the main payload area. It is designed to allow different experimental setups to be "flown" on the simulator. One of these experiments is the Revolve MBRotor magnetic bearing system, described in Appendix B. Additional information can be found in [26]*.

Figure A.1 is a picture of the Whorl–1 bottom deck during assembly. The thruster assembly is visible at the front. The nitrogen gas tank is mounted in the center. The bronze cube in front of the gas tank contains the attitude sensors.

*We update current developments on the Web at: http://www.aoe.vt.edu/research/groups/sssl. The DSACCS software is maintained at http://sourceforge.net/projects/dsacss

Figure A.1: *Whorl-1 with Magnetic Bearing on Top Deck*

The onboard computer is a 32–bit 133 MHz Tri-M MZ104+ ZFxd86 processor running a down–scaled version of the Linux operating system. The computer is based on the PC/104 form factor, has a 288 MB DiskOnChip solid-state memory and 64MB of RAM. It contains a 16–bit Diamond Systems DMM–32 A/D data acquisition board that is used to control the thrusters and process data measurements. The onboard computer can be accessed via wireless network cards. An identical computer is located on the top deck to interface with the MB350 magnetic bearing controller and facilitate the data collection during experiments. Currently, the only attitude sensor on Whorl–1 is the BEI MotionPack II. The MotionPak is a three–axis accelerometer and rate gyro package and is manufactured by Systron Donner.

The basic configuration of Whorl–1 contains two types of actuators for attitude control. The first is a set of three mutually perpendicular aluminum/steel wheels which can be used either in momentum wheel or reaction wheel mode. Each wheel is mounted on a SM3430 Smart Motor, has an axial inertia of 0.075 kg m^2 and a maximum angular momentum of 10 Nms. The second attitude control mechanism is the three–axis compressed gas thruster system. The solenoid thrusters are controlled via the onboard computer. The compressed nitrogen gas is stored in a tank located at the center of Whorl–1's bottom deck. Three linear actuators maintain the center of rotation of Whorl–1 by compensating for the loss in mass during thruster operations.

Figure A.2 shows a different view of the DSACSS bottom deck. In the front, we see one of the three wheels. The $\hat{b}_3$–axis linear actuator is visible above the wheel. The onboard computer is housed in the black enclosure located on the left edge of the bottom deck. The configuration in Figure A.2 includes the optional control–moment–gyro assembly, which can be seen at the back edge of Whorl–1. Finally, we note the structure of Whorl–2, the second spacecraft simulator in the plexiglass enclosure in the back of the room. Whorl–2 has just finished the design phase and is under construction.

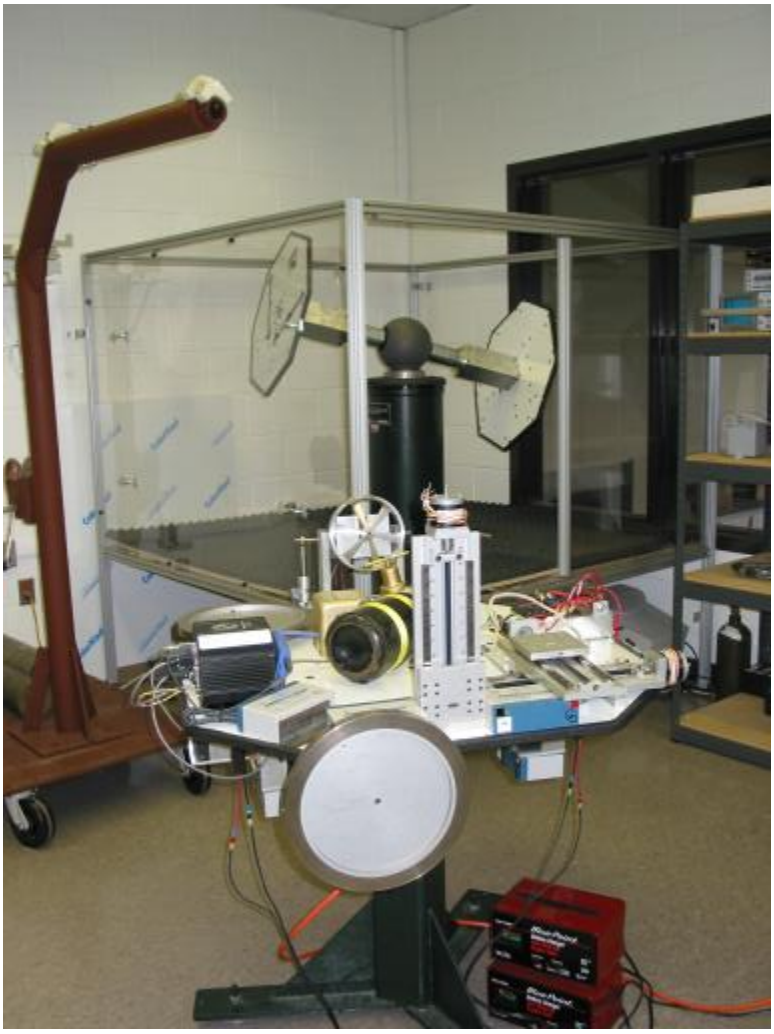

Figure A.2: *Whorl-1 with Magnetic Bearing on Top Deck*

Appendix B

MB Revolve Magnetic Bearing System

The Revolve MBRotor kit consists of two radial bearings and one thrust magnetic bearing. The radial bearings levitate the shaft and compensate for its radial motion. The thrust bearing actuates along the shaft axis giving the overall system three–axis control. The three bearings and the drive motor are mounted on an aluminum rail. The rail provides a solid base and its tracks keep all four components aligned. Misalignments, which are a major source of instability, are therefore avoided. The magnetic bearings support a shaft with one or more balancing wheels. The Rotor kit comes with three shafts. The shafts are 12", 18", and 25" in length and have a 3/8" diameter.

Although we previously used the term rotor to describe the entire shaft-wheel assembly, in this context, the term "rotor" refers to the silicon iron cylinder that fits inside the stator for each bearing and is mounted on the shaft. In addition to these rotors in each radial bearing, the MBRotor kit also provides balance disks that come with a 0.5" and 0.25" thickness. These disks have 16 holes drilled at a radius of 1.065" from the center. The purpose of these holes is to simplify balancing procedures. Figure B.1 shows the MBRotor kit. Some of the important specifications for all three bearings are listed in Tables B and B below.

A 48V electric motor provides the shaft's spin. The shaft is connected to the motor via a small flexible coupling. The coupling and the motor also provide support in the axial direction. For configurations with shorter shafts, the thrust bearing is sometimes omitted. The motor

Table B.1: *Radial Bearing Properties*

Radial Bearing Properties	**Value**
Number of wire turns per stator - N	137
Stator Pole Face Area - A_g	1.023 cm^2
Stator Outer Diameter	8.339 cm
Stator Inner Diameter	3.505 cm
Stator Stack Length	1.270 cm
Stator Material Grade	Silicon Iron
Rotor Outer Diameter	3.404 cm
Rotor Material Grade	Silicon Iron
Nominal Gap -g	0.0508 cm
Current Stiffness -K_i	45.68 N/Amp
Position Stiffness -K_x	228.3601 N/cm
Saturation Current -I_{sat}	3 Amp
Static Load Capacity	66 N
Dynamic Load Capacity (@250Hz)	66 N

and all three bearings are controlled by the MB350 controller/amplifier. The MB350 can be accessed via a front panel interface or remotely using an RS-422 serial connection. During normal bench–top operation the front panel access is usually sufficient. During experiments on Whorl–1 it is only possible to use the remote connection. We command the MB350 via a second PC/104 computer located on the top deck. This second computer both commands the MB350 and processes the data collected during experiments. Since the Tri-M MZ104+ uses a RS-232 serial standard, we require a RS422–RS232 converter between the two devices. The serial connection is only used to control the operation of the MB350. The experimental data are recorded using the analog channels of the DMM-32 data acquisition card. A small electronics board interfaces the 68-pin data output cable from the MB350 with the 50-pin ribbon cable of the DMM-32. During an experiment we collect the data and transmit them via the wireless ethernet to a desktop computer for analysis.

Figure B.1 shows both the MB350 and the rotor rig. The rig is configured with all three bearings, an 18" shaft and both balance disks. We note the MB350 front panel interface and display. The basic front panel options include motor direction and speed control. The position, current and force data can also be displayed. The gains of the active magnetic

Table B.2: *Thrust Bearing Properties*

Thrust Bearing Properties	**Value**
Number of wire turns per stator - N	238
Stator Pole Face Area - A_g	4.951 cm^2
Stator Outer Diameter	7.571 cm
Stator Inner Diameter	3.861 cm
Stator Stack Length	1.481 cm
Stator Material Grade	410-SS
Rotor Outer Diameter	6.604 cm
Rotor Material Grade	410-SS
Nominal Gap -g	0.0762 cm
Current Stiffness -K_i	55.78 N/Amp
Position Stiffness -K_x	3.52 N/cm
Saturation Current -I_{sat}	3 Amp
Static Load Capacity	80 N
Dynamic Load Capacity (@250Hz)	66 N

bearing are modified using the programs of the MBScope software suite. These Windows 98 based programs can be used to tune the controller settings or monitor and record the measured parameters.

Figure B.2 is a close–up view of the rotor rig. The 48V motor is mounted at the right end of the rail. Slightly to the left of the flexible coupling we see the speed sensor. Each shaft is notched on one end. The flat section of the notch is aligned in front of the speed sensor. The notch also acts as a key phasor for balancing purposes and is displayed in the Orbits tool of the MBScope software. The sensor itself is a Hall probe. Each of the radial magnetic bearings also contains a back–up ball–bearing. In the event of a magnetic bearing shutdown during operation the ball–bearings catches the shaft as it despins. The inner diameter of the ball–bearings is the limiting factor to the shaft's radial motion. Thus the back–up bearings protect the sensitive magnetic poles and position sensors which are inside the stators.

Figure B.3 and B.4 depict the partially assembled top–deck mounted on the Whorl–1 simulator. To the right of the rotor rig, in Figure B.3, we see the ExcelTech XP600 power inverter. Whorl–1 operates on a 24V bus. The MB350 and the MBRotor kit require stan-

Figure B.1: *Revolve MB350 and MBRotor Active Magnetic Bearing*

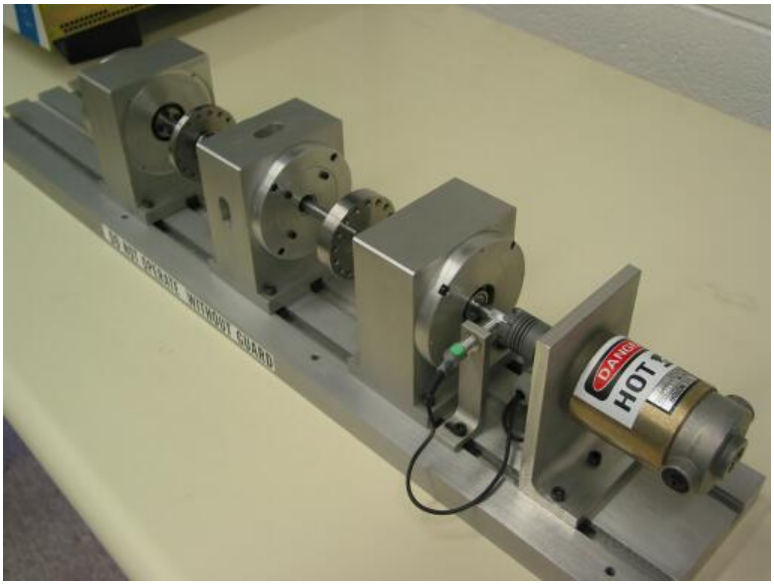

Figure B.2: *Revolve MBRotor Kit - Active Magnetic Bearing Assembly*

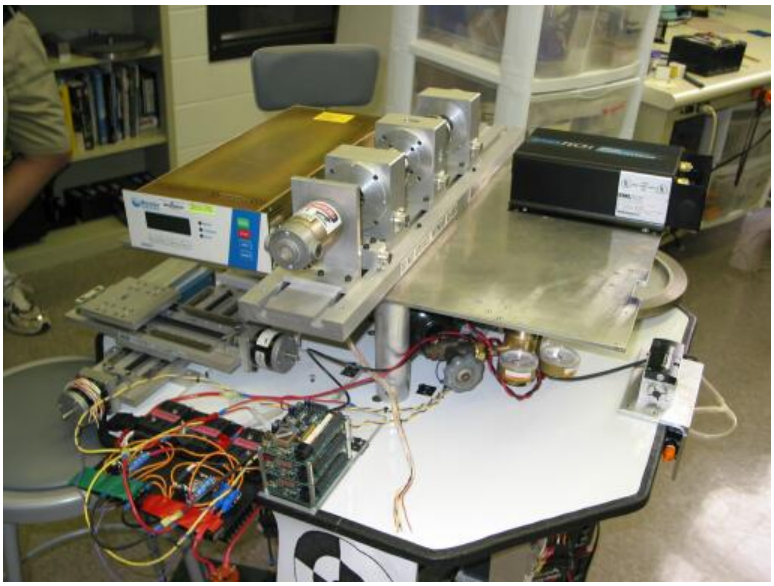

Figure B.3: *Active Magnetic Bearing with MB350 Controller on Whorl-1 Top Deck*

dard 120 VAC, thus depending on the inverter for power. The top deck computer, which is not shown in Figure B.3, is mounted in front of the inverter. During operation, a plexiglass cover protects the rotor rig and prevents any cables from interfering with the spinning shaft. Figure B.4 shows the same configuration from the back.

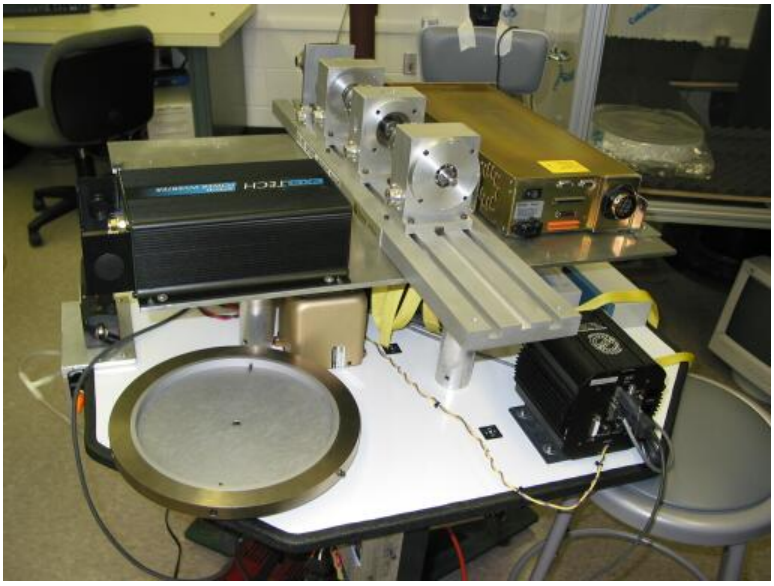

Figure B.4: *Active Magnetic Bearing with MB350 Controller on Whorl-1 Top Deck*

References

[1] E. Leimanis, *The General Problem of the Motion of Coupled Rigid Bodies about a Fixed Point*. New York: Springer Verlag, 1965.

[2] P. C. Hughes, *Spacecraft Attitude Dynamics*. New York: John Wiley & Sons, 1986.

[3] J. Wittenburg, "Beiträge zur Dynamik von Gyrostaten," Habilitationsschrift, Technische Universität Hannover, 1972.

[4] C. D. Hall and R. H. Rand, "Spinup Dynamics of Axial Dual-Spin Spacecraft," *Journal of Guidance, Control and Dynamics*, vol. 17, no. 1, pp. 30–37, January–February 1994.

[5] M. A. Plonus, *Applied Electromagnetics*. New York: McGraw-Hill, 1978.

[6] P. Allaire, E. Maslen, R. R. Humphris, C. K. Sortore, and P. A. Studer, "Low Power Magnetic Bearing Design for High Speed Rotating Machinery," (NASA, Langley Research Center), pp. 317–329, 1992.

[7] P. E. Allaire, E. H. Maslen, R. R. Humphris, C. R. Knospe, and D. Lewis, "Magnetic Bearings," in *Handbook of Lubrication and Tribology*, (New York), CRC Press, 1994.

[8] E. Maslen, P. Hermann, M. Scott, and R. R. Humphris, "Practical Limits to the Performance of Magnetic Bearings: Peak Force, Slew Rate, and Displacement Sensitivity," *ASME, Transactions, Journal of Tribology*, vol. 111, pp. 331–336, April 1989.

[9] K. Borstein, "Dynamic Load Capabilities of Active Electromagnetic Bearings," *ASME, Transactions,Journal of Tribology*, vol. 113, pp. 598–603, July 1991.

[10] R. Siegwart and A. Traxler, "Performance and Limits of AMB-Actuators Illustrated on a Electromagnetically Suspended Milling Spindle," in *Proceedings of the 25th Intersociety Energy Conversion Engineering Conference*, vol. 3, (New York), pp. 494–499, August 1990.

[11] D. K. Rao, G. V. Brown, P. Lewis, and J. Hurley, "Stiffness of Magnetic Bearings Subjected to Combined Static and Dynamic Loads," *ASME, Transactions, Journal of Tribology*, vol. 114, no. 4, pp. 785–789, October 1992.

[12] Revolve Magnetic Bearings Inc., Calgary, Alberta, Canada, *MBROTOR Research Test Stand Hardware User's Guide*, 893-0005 rev c 04/02 ed., 1998.

[13] Revolve Magnetic Bearings Inc., Calgary, Alberta, Canada, *MB350BT/MB350R Controller User's Guide*, 892-0031 revd 07/01 ed., 1998.

[14] J. L. Schwartz, M. A. Peck, and C. D. Hall, "Historical Survey of Air-Bearing Spacecraft Simulators," *Journal of Guidance, Control, and Dynamics*, vol. 26, no. 4, pp. 513–522, July–August 2003.

[15] J. R. Clements, "The Experimental Testing of an Active Magnetic Bearing/Rotor System Undergoing Base Excitation," Master's thesis, Virginia Tech, Blackburg, Virginia, 2000.

[16] A. Robinson, "Magnetic Bearings - The ultimate means of support for moving parts in space," *ESA Bulletin*, no. 26, pp. 14–19, May 1981.

[17] A. Robinson, "A lightweight, low cost, magnetic bearing reaction wheel for satellite attitude-control applications," *ESA Journal*, vol. 6, no. 4, pp. 397–406, 1982.

[18] M. Scharfe, K. Meinzer, and R. Zimmermann, "Development of a magnetic-bearing momentum wheel for the AMSAT Phase 3-D small satellite," in *Small satellites and services; Proceedings of the 3rd International Symposium*, no. A97-23887, (Annecy, France), June 1996.

[19] M. Scharfe, T. Roschke, E. Bindl, D. Blonski, and R. Seiler, "The challenges of miniaturisation for a magnetic bearing wheel," in *9th European Space Mechanisms and Tribology Symposium*, no. A02-45410, (Liege, Belgium), pp. 17–24, September 2001.

[20] P. F. Byrd and M. D. Friedman, *Handbook of Elliptic Integrals*. New York: Springer-Verlag, 1971.

[21] A. J. Turner and C. D. Hall, "An Open Source, Extensible Spacecraft Simulation and Modeling Environment Framework," in *Proceedings of the AAS/AIAA Astrodynamics Specialist Conference*, no. AAS 03-501, (Big Sky, Montana), August 2003.

[22] S. Sastry, *Nonlinear Systems Analysis,Stability, and Control*. New York: Springer Verlag, 1999.

[23] J.-J. E. Slotine and W. Li, *Applied Nonlinear Control*. Englewood Cliffs, New Jersey: Prentice Hall, 1991.

[24] F. F. Ehrich, *Hand Book of Rotordynamics*. Malabar, Florida: Krieger, 1999.

[25] M. E. Leader, "Practical Rotor Dynamics for Turbomachinery," *ASME Turbomachinery Course Notes*, April 1983.

[26] J. L. Schwartz and C. D. Hall, "The Distributed Spacecraft Attitude Control System Simulator: Development, Progress, Plans," in *Proceedings of the Flight Mechanics Symposium*, (NASA Goddard Space Flight Center, Greenbelt, Maryland), October 28–30 2003.

Vita

Marcus Pressl was raised near Nuremburg, Germany. After finishing his secondary education Langenzenn, Germany, he studied Mechanical Engineering at Purdue University in West Lafayette, Indiana, where he received a B.S.M.E. degree in 1995. The summer following graduation he became a Peace Corps volunteer and spend the next two and a half years in Benin, West Africa, teaching mathematics at a rural high school. Having gone all the way to Africa, Marcus found his greatest treasure, his wife to be, Cheryl. After both returned to the U.S., Marcus worked two years as a HVAC design engineer at Metropolitan Engineering Inc. in Washington D.C., while his wife was completing a degree in Moral Theology. They were married in Crested Butte, Colorado in the summer of 1999. They then moved to Blacksburg, Virginia, where Marcus pursued a Master of Science degree in Aerospace Engineering. During his studies, he helped with the design and construction of HokieSat and also participated in the construction of Virginia Tech's spacecraft simulators.